Dissertations   Graduate College

6-2019

Development of Heat Transfer Correlations for Low-Reynolds Numbers, Flows in Horizontal Circular Pipes

Latif Eyada Ibraheem
Western Michigan University, latif.ibraheem@gmail.com

DEVELOPMENT OF HEAT TRANSFER CORRELATIONS FOR LOW-REYNOLDS NUMBERS,
FLOWS IN HORIZONTAL CIRCULAR PIPES

by

Latif Eyada Ibraheem

A dissertation submitted to the Graduate College
in partial fulfillment of the requirements
for the degree of Doctor of Philosophy
Mechanical Engineering
Western Michigan University
May 2019

Doctoral Committee:

Claudia Fajardo-Hansford, Ph.D., Chair
Parviz Merati, Ph.D.
HoSung Lee, Ph.D.
Christopher Cho, Ph.D.
David Meade, Ph.D.

ACKNOWLEDGEMENTS

DEVELOPMENT OF HEAT TRANSFER CORRELATIONS FOR LOW-REYNOLDS NUMBERS, TRANSITIONAL FLOWS IN HORIZONTAL CIRCULAR PIPES

Latif Eyada Ibraheem, Ph.D.

Western Michigan University

Turbulent flows are intrinsic to most fluid-based engineering systems, including internal combustion engines. In these devices, mixing, scalar transport and heat transfer are both critical for proper operation and challenging to model. In previous work, Kreun et al. [1] modeled a pre-heated intake manifold of a Diesel engine for cold-start simulations. Accurately predicting the heat transfer at the intake port proved to be a challenging task. Existing heat transfer correlations yielded predictions which were (at best) within 20% of the measured values. The discrepancy was attributed to a mismatch between the range of applicability of existing heat transfer models and cold-cranking conditions. This is because the intake runners are typically not long enough for the flow to fully develop and cranking speeds are not high enough to induce a wholly turbulent gas flow. Accurately predicting heat transfer in non-fully developed, transitional flows remains a difficult task. While several empirical correlations have been developed for turbulent, fully-developed flow at $Re > 10^4$, many applications rely on flows in transition, spanning a range of $2300 < Re < 10^4$, as well as low Reynolds number turbulent flows. In this regime, most of the correlations are based on interpolated values with very limited direct measurements. Hence, there is a need for accurate heat transfer correlations based on direct velocity and temperature measurements for transitional and low Reynolds numbers turbulent flows.

To address this need, simultaneous flow-field/heat transfer measurements were conducted to develop correlations for calculating the Nusselt number (hence the convective heat transfer coefficient) for low-Reynolds number flows, and under steady-state constant heat flux conditions. Measurements of temperature and velocity were conducted for *combined entry*, which refers to a simultaneously (thermally and hydrodynamically) developing flow. Three experimental configurations were investigated: uniform, tripped flow, and ninety-degree entrance. These conditions were explored both to test the range of applicability of the developed correlations and to replicate conditions that might be found in reciprocating internal combustion engine runners. Experimental results were correlated in terms of the governing dimensionless numbers to develop an accurate model for heat transfer for the targeted regime and pipe lengths.

TABLE OF CONTENTS

Table of Contents--Continued

Table of Contents--Continued

LIST OF TABLES

LIST OF FIGURES

CHAPTER I

BACKGROUND

1.1   Introduction

Quantifying heat transfer phenomena near the entrance of horizontal circular pipes for air flows at low-Reynolds numbers is a complex problem. In this regime, flows are highly sensitive to secondary flows induced, for example, by separation and buoyancy effects [3] [4]. Generally, a hydrodynamically fully-developed laminar flow is an ideal laboratory condition. Laminar flows are disrupted once the Reynolds number exceeds approximately 2300 and start the transition to turbulence. In practice, the presence of sharp edges, bends, fans, valves, and abrupt boundary changes induce secondary flows at relatively low Reynolds numbers. In addition, surrounding noise, and vibration can, in practice, shift the Reynolds number at which transition occurs, triggering the onset of turbulence [3]. In this case, significantly higher heat transfer rates have been observed and attributed to flow separation and vorticity effects [3] [4]. In addition, the secondary flows generated by free convection enhance the heat transfer coefficients in horizontal circular tubes and increase the critical Reynolds number for the laminar-to-turbulent transition.

1.2   Fluid Flow and Heat Transfer Parameters

In order to characterize the air flow in horizontal circular pipes and study the associated heat transfer phenomena, it is convenient to use specific parameters and dimensionless groups. All

the parameters needed are introduced in this section. Dimensionless groups are summarized in table 1.1.

The dimensionless axial distance x^+ for the hydrodynamically developing flow is defined as

$$x^+ \equiv \frac{x/D}{Re} \qquad (1.1)$$

Where,

$x \equiv$ axial distance

$D \equiv$ pipe diameter

And Re is Reynolds number, defined as

$$Re \equiv \frac{u_m D}{\nu} \qquad (1.2)$$

$u_m \equiv$ Flow mean velocity defined in equation 1.3

$\nu \equiv$ The fluid kinematic viscosity.

$$u_m = \frac{2}{r_o^2} \int_0^{r_o} u(r, x) r dr \qquad (1.3)$$

In the mean velocity equation 1.3, r_o is the pipe radius.

The *fanning friction factor f* is defined as the ratio of the wall shear stress τ_w to the flow kinetic energy per unit volume, $\rho u_m^2 / 2$,

$$f \equiv \frac{\tau_w}{\rho u_m^2 / 2} \qquad (1.4)$$

Meanwhile, the apparent fanning friction factor is:

$$f_{app} \equiv \left(\frac{p_o - p}{\rho u_m^2 / 2} \right) \left(\frac{r}{x} \right) \qquad (1.5)$$

Where p_o is the air static pressure at the entrance of the pipe $(x = 0)$ and p in the air static pressure at the point of interest.

The bulk mean temperature is defined as:

$$T_m = \frac{2}{u_m r_o^2} \int_0^{r_o} uTr dr \qquad (1.6)$$

The local axial heat transfer coefficient h_x is defined as

$$h_x \equiv \frac{q_w''}{(T_w - T_m)} \qquad (1.7)$$

T_w is the pipe wall temperature (circumferentially averaged) and q_w'' is the heat flux.

The integrated average heat transfer coefficient from the pipe entrance $(x = 0)$ to any axial distance x is given as

$$h_m = \left(\frac{1}{x}\right) \int_0^x h_x \, dx \qquad (1.8)$$

The local Nusselt number is shown in equation 1.9, where k is the fluid's thermal conductivity.

$$Nu_x \equiv \frac{h_x D}{k} \qquad (1.9)$$

The average Nusselt number is

$$Nu_m = \left(\frac{1}{x}\right) \int_0^x Nu_x \, dx \qquad (1.10)$$

The dimensionless axial distance for a thermally developing flow is shown in equation 1.11, where Pr is the Prandtl number equation 1.12.

$$x^* \equiv \frac{x/D}{RePr} \qquad (1.11)$$

$$Pr \equiv \frac{\nu}{\alpha} \qquad\qquad\qquad (1.12)$$

$\alpha \equiv$ thermal diffusivity

$\rho \equiv$ fluid density

$\tau_w \equiv$ wall shear stress

Throughout this document, the acronyms *UWT* and *UHF* will be used to refer to the *uniform wall temperature* and *uniform heat flux* boundary conditions, respectively. Table 1.1 lists the non-dimensional parameters relevant to this work, along with their physical significance. Several terms used throughout the document are defined as follows:

- *Combined entry length:* distance over which both the thermal and hydrodynamic boundary layers develop simultaneously.

- *Thermal entry length:* length over which the flow is thermally developing in an already hydrodynamically fully-developed flow.

- *Transitional flows:* those for which the Reynolds number approximately lies between 2300 and 10,000 (i.e., $2300 \leq Re \leq 10^4$).

Table 1.1: The non-dimensional groups relevant to heat transfer correlations

Dimensionless Group	Definition	Physical Description
Reynolds number	$$Re = \frac{UD}{\nu}$$	Ratio of inertia to viscous effects
Local Nusselt number	$$Nu_x = \frac{h_x D}{k}$$	Ratio of convective conductance to pure molecular thermal conductance
Prandtl number	$$Pr = \frac{\nu}{\alpha}$$	Ratio of momentum diffusivity to thermal diffusivity of the fluid
Grashof number	$$Gr = \frac{g\beta\Delta T D^3}{\nu^2}$$	Ratio of buoyancy to viscous force acting on the fluid
Rayleigh number	$$Ra = GrPr$$	Ratio of natural convective to diffusive heat transfer
Graetz Number	$$Gz_D = \left(D/x\right)Re_D\,Pr$$	Ratio of thermal capacity to convective heat transfer
Richardson	$$Ri = \frac{Gr}{Re^2}$$	Ratio of buoyancy to inertial force
Turbulence intensity	$$\frac{\sqrt{\frac{1}{N}\sum_{i=1}^{N}(u')^2}}{\bar{u}}$$	Ratio of the Root-Mean-Square (RMS), of the turbulent velocity to the mean velocity, where $u' = u - \bar{u}$

CHAPTER 2

LITERATURE REVIEW: HEAT TRANSFER BY CONVECTION

2.1   Heat Transfer in Fully Developed Flow

2.1.1   Fully Developed Laminar Flow

Fully developed laminar flow in pipes occurs when the particles of the fluid move in uniform paths parallel to the pipe axis. The velocity profile is parabolic, it reaches a maximum at the pipe centerline and decreases in the radial direction, reaching zero at the walls [3]. Theoretical solutions for fully-developed laminar flows inside circular pipes can be obtained assuming incompressible flow, constant fluid properties and only axial advection of thermal energy. The convection heat transfer for constant surface heat flux is determined from the temperature distribution resulting from the solution of the governing differential equation 2.1 [5]. The convection heat transfer for UHF is given by equation 2.2 and for UWT by equation 2.3.

$$u\frac{\partial T}{\partial x} = \frac{\alpha}{r}\frac{\partial}{\partial r}\left(r\frac{\partial T}{\partial r}\right)$$ (2.1)

$$Nu = \frac{hD}{k} = 4.36$$ (2.2)

$$Nu = \frac{hD}{k} = 3.66$$ (2.3)

2.1.2   Fully Developed Turbulent Flow

Turbulent flow results from random fluid motion [3]. Unfortunately, there is no analytical deterministic solution available for turbulence problems. Hence, empirical models, statistical

analysis, and direct numerical simulations are the available methods to predict turbulence quantities and their evolution [6]. The Colburn equation 2.4 provides an estimate of the heat transfer coefficients *in fully hydrodynamically and thermally developed flows*. This correlation is applicable for small to moderate temperature differences $(T_s - T_m)$, Prandtl numbers in the range of $0.6 \leq Pr \leq 160$, $\frac{L}{D} \geq 10$ and Reynolds numbers (Re) above 10,000. Within this range, the heat transfer depends on Reynolds and Prandtl numbers [5].

$$Nu_D = 0.023Re_D^{4/5}Pr^{1/3} \qquad (2.4)$$

$Nu_D \equiv$ average Nusselt number

$Re_D \equiv$ Reynolds number

$Pr \equiv$ Prandtl number

$T_s \equiv$ pipe surface temperature

$T_m \equiv$ mean fluid temperature

The Dittus and Boelter correlation, also applicable in this regime, is shown in equation 2.5 [7], where n=0.4 for heating and 0.3 for cooling. Dittus' and Boelter' correlation was developed using three oils with a wide viscosity range.

$$Nu_D = 0.023Re_D^{4/5}Pr^n \qquad (2.5)$$

When the fluid properties change significantly near the wall, the correlation developed by Sieder and Tate, shown in equation 2.6, is recommended [8].

$$Nu_D = 0.023Re_D^{4/5}Pr^{1/3}\left(\frac{\mu_m}{\mu_s}\right)^{0.14} \qquad (2.6)$$

In this equation,

$\mu_m \equiv$ viscosity of the fluid evaluated at T_m

$\mu_s \equiv$ viscosity of the fluid evaluated at T_s

Hence, the correlations for the fully-developed turbulent flow depend on Reynolds and Prandtl numbers.

2.1.3   Fully Developed, Laminar-to-Turbulent Transition Flow

The Reynolds number is used as a metric to quantify the laminar to turbulent flow transition.

Typically, for internal (pipe) flow the upper and lower bounds for laminar and turbulent flows are

given as 2300, and 10^4, respectively, such that when $2300 \leq Re \leq 10^4$, the flow might still be in

transition. It is significant to point out, however, that these bounds depend on the pipe entrance

geometry, wall roughness, flow type (e.g., pulsating as in an IC engine manifold) and surrounding

noise, vibrations, and buoyancy effects. However, the lower Reynolds number limit of 2300 is

widely accepted for the beginning of the transition and the highest limit is typically defined as

10^4 [3] [2]. Correlations for heat transfer coefficients in both fully developed laminar and

turbulent regimes are fully established in the literature. Meanwhile, the transition region is still

a field of ongoing development. A few examples follow.

Churchill [9] and Gnielinski [10], separately introduced general heat transfer correlations

equations 2.7 through 2.11, based on interpolation between the available theoretical

correlations for laminar flow and empirically-developed correlations for turbulent flow.

Churchill's correlation is given in equation 2.7.

$$(Nu)^{10} = (Nu_l)^{10} + \left\{ \frac{e^{(2200-Re)/365}}{(Nu_l)^2} + \frac{1}{(Nu_t)^2} \right\} \qquad (2.7)$$

$$Nu_t = Nu_o + \frac{0.079(\frac{f}{2})^{1/2}RePr}{(1 + Pr^{\frac{4}{5}})^{5/6}} \qquad (2.8)$$

$Nu_o = 4.8$ for UWT and 6.3 for UHF

$Nu_l = 3.657$ for UWT and 4.364 for UHF

This general correlation covers the entire range of transition from laminar to turbulent flows in smooth pipes for $10 \leq Re \leq 10^6$ and $Pr > 100$. For $Re \leq 2300$, Churchill's correlation gives the laminar flow values of Nu. For $2100 \leq Re \leq 10^4$ it gives Nu values for transitional flow. For the range $10^4 \leq Re \leq 10^6$ and $0.5 \leq Pr \leq 2000$ Churchill correlation agrees with Gnielinski's (discussed next) within +17.1% and − 11.9% for the constant wall temperature boundary condition and within +13.7% and -10.5% for the constant heat flux boundary condition [3]. Gnielinski's correlations (2.9-2.11) which are applicable for $2300 \leq Re \leq 5x10^6$ and $0.5 \leq Pr \leq 2000$, are mostly accepted in practice for the transition regime. However, it has been suggested [11] [3] that its use is restricted to $Re > 4000$, due to lack of the friction factors for $Re < 4000$ required for Gnielinski correlation.

$$Nu = \frac{\left(f/2\right)(Re - 1000)Pr}{1 + 12.7\left(\frac{f}{2}\right)^{\frac{1}{2}}(Pr^{\frac{2}{3}} - 1)} \qquad (2.9)$$

$2300 \leq Re \leq 5x10^6, 0.5 \leq Pr \leq 2000$

$$Nu = 0.0214(Re^{0.8} - 100)Pr^{0.4} \qquad (2.10)$$

$10^4 \leq Re \leq 5x10^6, 0.5 \leq Pr \leq 1.5$

$$Nu = 0.012(Re^{0.87} - 280)Pr^{0.4} \tag{2.11}$$

$$3x10^3 \leq Re \leq 10^6, 1.5 \leq Pr \leq 500$$

Ghajar and Tam [12] experimentally investigated the heat transfer in the entrance of a 1.48 cm-diameter circular pipe using different mixtures of ethylene glycol and water. Three inlet configurations were considered: reentrant, square-edged and bell-mouth. The heat transfer correlations developed from their work, shown in equations 2.12-2.16, are valid for $280 < Re < 49,000$ and $4 < Pr < 158$. The temperature distribution inside the pipe in this study was predicted using a finite difference computer program from a separate study relying on wall temperature measurements [13].

$$Nu_l = 1.24 \left[\frac{RePr}{x/D} + 0.024(GrPr)^{0.75} \right] \left(\frac{\mu_m}{\mu_w} \right) \tag{2.12}$$

Equation 2.12 is applicable to combined entrance and fully developed laminar flow for forced and mixed convection, with $280 \leq Re \leq 3800$, $40 \leq Pr \leq 160$, $1000 \leq Gr \leq 2.8x10^4$, $3 \leq x/D \leq 192$ and $1.2 \leq \frac{\mu_m}{\mu_w} \leq 3.8$. For the transition regime, Ghajar suggested the correlation shown in equation 2.13,

$$Nu_{tr} = Nu_l + [\exp\left(\frac{a - Re}{b}\right) + Nu_t^c]^c \tag{2.13}$$

where Nu_l and Nu_t are obtained from equations 2.12 and 2.14 respectively. The parameters a, b and c are constants dependent on the inlet configuration and given for reentrant (disturbed flow) as

$$a = 1766, b = 276, \; c = -0.955$$

$$1{,}700 \leq Re \leq 9{,}100, \;\; 5 < Pr < 51, \;\; 4000 \leq Gr \leq 2.1x10^5,$$

$$1.2 \leq \frac{\mu_m}{\mu_w} \leq 2.2,, \;\; 3 \leq x/D \leq 192$$

and for a square-edged inlet as

$$a = 2617, b = 207, \; c = -0.950$$

$$1{,}600 \leq Re \leq 10{,}700, \;\; 5 \leq Pr \leq 55, \;\; 4000 \leq Gr \leq 2.5x10^5,$$

$$1.2 \leq \frac{\mu_m}{\mu_w} \leq 2.6, \; 3 \leq x/D \leq 192$$

For a bell-mouth inlet the constants are:

$$a = 6628, b = 237, \; c = -0.980$$

$$3{,}300 \leq Re \leq 11{,}100, \;\; 13 \leq Pr \leq 77, \;\; 6000 \leq Gr \leq 1.1x10^5,$$

$$1.2 \leq \frac{\mu_m}{\mu_w} \leq 3.1, \;\; 3 \leq x/D \leq 192$$

The turbulent correlation is

$$Nu_t = 0.023Re^{0.8}Pr^{0.385}\left(\frac{x}{D}\right)^{-0.0054}\left(\frac{\mu_m}{\mu_w}\right)^{0.14} \tag{2.14}$$

$$7000 \leq Re \leq 49{,}000, \; 4 < Pr < 34,$$

$$1.2 \leq \frac{\mu_m}{\mu_w} \leq 3.1, \;\; 3 \leq x/D \leq 192$$

2.2 Convection Heat Transfer in Thermal Entry

The thermal entry problem refers to the condition of a thermally developing profile under a hydrodynamically fully developed velocity profile. Practically, the thermal entry condition can be

established using a long calming section upstream of the heated area. In laminar flow, this is so called the Graetz problem. Hausen [14] suggested the correlation given in equation 2.15 for the mean Nusselt number, where x^* is the dimensionless axial distance for a thermally developing flow. The predicted values of Nu from equation 2.15 are 14% higher than the theoretically calculated values for $x^* < 0.0001$ and fit smoothly with theoretical values for $x^* \to \infty$ [3]

$$Nu_m = 3.66 + \frac{0.0668}{x^{*1/3}(0.04 + x^{*2/3})} \tag{2.15}$$

For turbulent flows, heat transfer in the thermal entry region has been investigated quite extensively. Al-Arabi [15] provided correlation to calculate the mean Nu for thermally developing flows under UWT and UHF. Al-Arabi's correlation is discussed in more detail in section (2.4).

2.3   Convection Heat Transfer in Combined Entry

2.3.1   Laminar Flow in Combined Entry

Both velocity and thermal profiles may develop simultaneously in the pipe entrance region if they are uniform at the pipe inlet. This phenomenon is referred to as the combined entry length. Higher heat transfer coefficients have been quantified for this condition relative to the fully developed flow. The increase has been attributed to the high-velocity gradients near the walls, which convect more heat in the axial direction. The thermal boundary layer grows faster for higher Prandtl numbers in this regime [2]. The theoretical solution for simultaneously hydrodynamically- and thermally- developing laminar flows is very complicated. The velocity and temperature profiles depend on the radial and axial directions [5]. Equation 2.16 was suggested for the condition of combined thermal and velocity entry lengths and constant wall temperature [16]. Secondary flows in the entrance region, which may be induced by flow separation or

buoyancy are not considered in theoretical relations. Theoretically predicted Nusselt numbers, in this case, are lower than the experimentally measured values [2].

$$\overline{Nu_D} = \frac{\dfrac{3.66}{tanh[2.264\ Gz_D^{-1/3} + 1.7\ Gz_D^{-2/3}]} + 0.0499\ Gz_D\ tanhGz_D^{-1}}{tanh(2.432\ Pr^{1/6}\ Gz_D^{-1/6}} \qquad (2.16)$$

Where,

$$Gz_D = \left(D/x\right)Re_D\ Pr \quad \text{(Graetz Number)}.$$

An experimental correlation that is applicable to combined entry laminar flow has been proposed by Ghajar [12], as shown in section 2.1.3, equation 2.12. We note that, in the entrance region, the Nusselt number depends on the Graetz number because of the axial distance parameter (x/D).

2.3.2   Turbulent Flow in Combined Entry

The problem of thermally- and hydrodynamically-developing fully turbulent flow in smooth pipes has been solved theoretically by Deissler [17] for $Pr = 0.73$ for both isothermal and uniform heat flux boundary conditions. He used the integral heat transfer and momentum equations to calculate the thickness of the thermal and hydrodynamic boundary layers. Deissler equations cover $Re > 10^4$ and $L/D < 8$. Figure 2.1 shows local Nusselt numbers for various Reynolds numbers and both isothermal and uniform heat flux boundary conditions.

An empirical correlation for the prediction of the average Nusselt number in turbulent flows was experimentally developed by Molki and Sparrow [18]. This correlation, shown in equations 2.17

and (2.18), is applicable to circular tubes as short as two diameters with sharp entrance edges and simultaneously developing (thermal and hydrodynamic) boundary layers at $Re \geq 10,000$.

$$\frac{Nu_m}{Nu_{fd}} = 1 + a/(X/D)^b \tag{2.17}$$

$$a = 23.99Re^{-0.23}, \qquad b = -2.08 \times 10^6 Re + 0.815 \tag{2.18}$$

Where, Nu_m is the average Nusselt number, over the length x of the pipe. Nu_{fd} refers to fully-developed Nusselt number and D is the pipe diameter. The constants a and b, which are functions of the Reynolds number, were obtained by a least-square fit to the experimental data.

2.4   Inlet Geometry Effects

The shape and configuration of the pipe inlet have substantial effects on the simultaneously developing flow. Heat transfer coefficients are significantly higher due to secondary flows generated from boundary layer separation [3] [2]. Boelter [19] comprehensively investigated the influence of the entrance geometry on heat transfer coefficients. Sixteen different configurations were considered, with air entering circular smooth pipes for $Re \approx 5 \times 10^4$. Figure 2.2 shows results from Boelter's study.
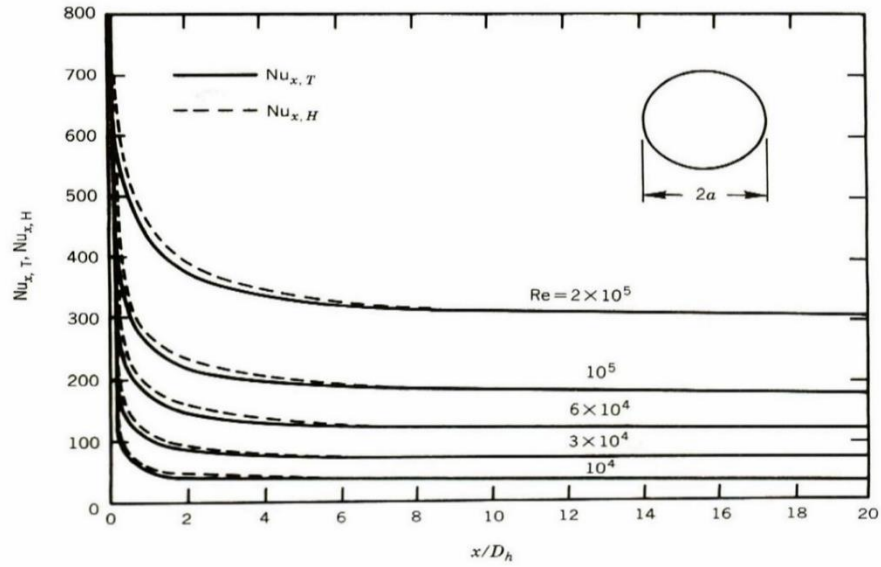
Figure 2.1 Local Nusselt numbers for simultaneously developing turbulent flow obtained by Deissler [17]
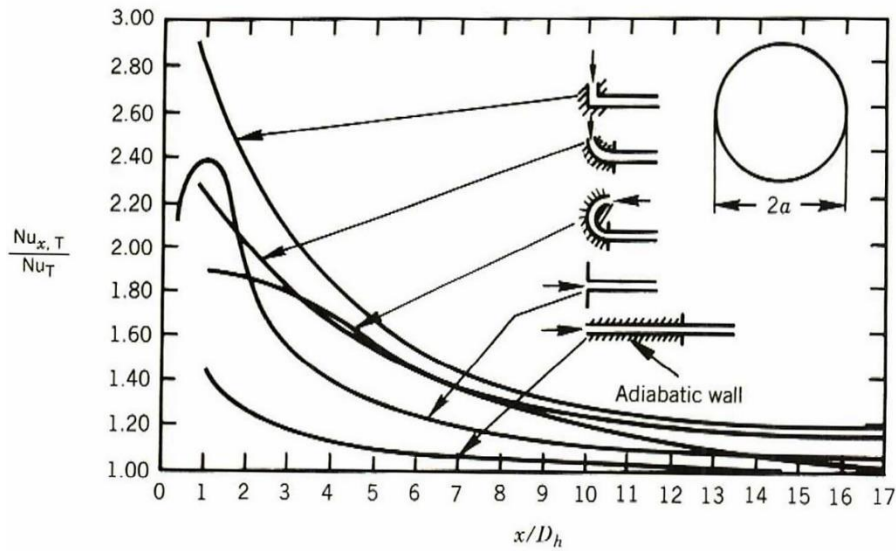
Figure 2.2 Local Nusselt numbers for turbulent flow in the entrance of
smooth circular pipes with different entrance configurations for Re$\approx 5 \times 10^4$, $Pr = 0.7$ [19]

Mills [20] experimentally investigated turbulent air flow in the entrance region of a circular pipe covering Reynold numbers from 10,000 to 110,000 and entrance lengths of $\frac{1}{4} < \frac{L}{D} < 320$. Local heat transfer coefficients were obtained for uniform wall heat flux considering many entrance configurations such as a long calming section, bell-mouth, orifice plate elbow, and T-piece. Al-

15

Arabi [15], suggested different correlations to calculate the shape factor S to correlate the available experimental data using a Boelter's equation 2.19. Various flow conditions and inlet geometries (sharp edge, ninety-degree angle bend) and tube sheet thickness were considered in that study. Al-Arabi's correlation is valid for fully developed, uniform, thermal and combined entry turbulent flows for circular pipes.

$$\frac{h_L}{h_\infty} = 1 + S\left(\frac{x}{D}\right)^n \tag{2.19}$$

$h_L \equiv$ local heat transfer coefficient.

$h_\infty \equiv$ heat transfer coefficient for fully developed flow.

$S \equiv$ correlation factor

Al-Arabi found that the S factor varies with Re, x/D and Pr in the fully developed condition. The suggested correlation in equation 2.20 is valid for fully developed flow in the entrance region for air, water, and oil for $5,000 \le Re \le 110^5$, $0.7 \le Pr \le 75$, $x/D > 3$, with up to 30% error at the lower Reynolds number end.

$$\frac{SPr^{1/6}}{\left(x/D\right)^{0.1}} = 0.68 + \frac{3000}{Re^{0.81}} \tag{13.20}$$

In contrast, S will depend on x/D only for non fully-developed turbulent flows at the tube entrance. For a sharp-edge entrance, the S factor and the local heat transfer correlations are given in equations 2.21 and 2.22

$$S = 1.683\left(\frac{x}{D}\right)^{0.423} \tag{2.21}$$

$$\frac{h_L}{h_\infty} = 1 + \frac{1.683}{\left(\frac{x}{D}\right)^{0.577}} \tag{2.22}$$

These equations are valid for air and water with $Re > 7{,}000$ and $\frac{x}{D} > 3$; and for ninety- degree entrance, with $Re > 8{,}000$ and $\frac{x}{D} > 5$

This literature review revealed that the available heat transfer correlations for the combined velocity and thermal entrance region in circular pipes in the transition and low Reynolds number turbulent regimes are scarce and estimated mostly based on interpolation. There is lack of direct experimental measurements of mean velocity, turbulence intensity, and temperature, from which direct heat transfer correlations may be empirically derived. The various correlations examined as part of this literature review and previously discussed are listed in table 2.1. Applicability conditions and restrictions for these correlations are summarized in table 2.2. From table 2.2, four correlations are applicable for transitional and low Reynolds number turbulent flows: Churchill's, Hausen's, Gnielinski's and Ghajar. However, only Gnielinski's and Ghajar's correlations are applicable for combined entry. Gnielinski's correlation spans Reynolds numbers above 4,000 and, as previously mentioned, was developed by interpolating experimental data for both transition and fully- developed flow. Ghajar's correlation is only applicable only Pr > 5, as shown in table 2.1.

2.5   Goal and Objectives

The goal of this research is to develop accurate heat transfer correlations based on direct velocity and temperature measurements. Specifically, these correlations will yield heat transfer

coefficients that can be used in practice to quantify the heat transfer in the entrance region of horizontal, short circular pipes (x/D ~ 6) under uniform heat flux, for air at Reynolds numbers ranging from 2,900 to 50,000 for combined entry conditions.

Three inlet configurations have been investigated: uniform flow, tripped flow, and ninety-degree elbow entry.

The main motivation is to fill a knowledge gap in this area, as identified through the literature review. A secondary motivation is to target regimes of interest for internal combustion engine (and other practical) applications.

Table 2.1: The heat transfer correlations				
Investigators	**Correlations**	**Flow condition based on Applicability Range (column 3) and Condition for Best Accuracy (if available)**	**Type**	**Proposed Applicability Range Re, Ra, x*, Gz or Ri range**	**Pr range**
Classic [5]	$Nu = \dfrac{hD}{k} = 4.36$	Laminar, fully developed, uniform heat flux, L/D> 0.05RePr	Theoretical	Re< 2300	Pr>0
Classic [5]	$Nu = \dfrac{hD}{k} = 3.66$	Laminar, fully developed, uniform wall temperature, L/D> 0.05Re	Theoretical	Re< 2300	Pr>0
Baher [16]	$\overline{Nu_D} = \dfrac{\dfrac{3.66}{tanh[2.264\,Gz_D^{-1/3} + 1.7\,Gz_D^{-2/3}]} + 0.0499\,Gz_D\,tanhGz_D^{-1}}{tanh(2.432\,Pr^{1/6}\,Gz_D^{-1/6}}$	Laminar and turbulent, combined entry, uniform surface temperature, 0.25< L/D<320	Empirical	10^4< Re<11x10^4	0.7
Colburn [5]	$Nu_D = 0.023Re_D^{4/5}Pr^{1/3}$	Turbulent, fully developed	Empirical	10^4<Re<10^5	0.6-160
Dittus and Boelter [7]	$Nu = 0.023Re^{0.8}Pr^n$ n= 0.4 for heating and 0.3 for cooling	Transition, turbulent fully developed ($\frac{L}{D} \geq 10$)	Empirical	2500<Re< 1.24x10^5	0.7-120
Deissler [17]	$Nu = 0.0789\,Re\sqrt{f}Pr^{1/4}$	Turbulent, developing velocity and thermal profiles	Empirical	5x10^3<Re <3x10^5	Pr>200
Sieder and Tate [8]	$Nu = 0.027Re^{4/5}Pr^{1/3}(\dfrac{\mu_m}{\mu_w})^{0.14}$	Turbulent, fully developed	Empirical	800<Re< 22,000	4-158
Mills [20]	$Nu = 0.0397Re^{0.73}Pr^{0.33}$	Turbulent flow, entry region, uniform heat flux, 0.25<L/D<320	Empirical	10^4<Re< 11x10^4	0.7
Churchill [9]	$(Nu)^{10} = (Nu_l)^{10} + \left\{ \dfrac{e^{(2200-Re)/365}}{(Nu_l)^2} + \dfrac{1}{(Nu_t)^2} \right\}$	Laminar fully developed, transition	Empirical	10<Re<10^6	
	$Nu_t = Nu_o + \dfrac{0.079(\frac{f}{2})^{1/2}RePr}{(1 + Pr^{\frac{4}{5}})^{5/6}}$	Turbulent, fully developed			Pr>100
	$Nu_o = 4.8$ for UWT and 6.3 for UHF $Nu_l = 3.657$ UWT and 4.364 for UHF				
Molki and Sparrow [18]	$\dfrac{\overline{Nu}}{Nu_{fd}} = 1 + a/(X/D)^b$ $a = 23.99Re^{-0.23}$, $\quad b = -2.08 \times 10^6 Re + 0.815$	Turbulent, combined entry, L/D$\geq$ 2	Empirical	5000<Re<88,000	2.5
Al-Arabi [15]	$\dfrac{h_L}{h_\infty} = 1 + S\left(\dfrac{x}{D}\right)^n$ $\dfrac{SPr^{1/6}}{(x/D)^{0.1}} = 0.68 + \dfrac{3000}{Re^{0.81}}$	General form for combined entry Fully developed flow in the entrance $x/D > 3$ Sharp edge entrance with $x/D > 3$	Empirical		
				5x10^3<Re<1x10^5	0.7-75

Table 2.1—Continued

20

	$S = 1.683\left(\frac{x}{D}\right)^{0.423}$ $\frac{h_L}{h_\infty} = 1 + \frac{1.683}{\left(\frac{x}{D}\right)^{0.577}}$ $S = 2.8\left(\frac{x}{D}\right)^{0.2}$ $\frac{h_L}{h_\infty} = 1 + \frac{2.8}{\left(\frac{x}{D}\right)^{0.8}}$	Ninety- degree entrance w $x/D > 3$		$Re > 7,000$ $Re > 8,000$	
Gnielinski [10]	$Nu = \frac{\left(\frac{C_f}{2}\right)(Re - 1000)Pr}{1 + 12.7\left(\frac{C_f}{2}\right)^{0.5}\left(Pr^{\frac{2}{3}} - 1\right)}\left[1 + \left(\frac{D}{X}\right)^{\frac{2}{3}}\right](\frac{\mu_m}{\mu_w})^{0.14}$ $Nu = 0.0214(Re^{0.8} - 100)Pr^{0.4}$ $Nu = 0.021(Re^{0.87} - 280)Pr^{0.4}$	Transition, turbulent, combined entry Most accurate at Re> 4000 Transition, turbulent fully developed Transition, turbulent fully developed	Empirical	$2,300<Re<5\times10^6$ $10^4<Re<5\times10^6$ $3\times10^3<Re<10^6$	0.5-2,000 0.5-1.5 1.5-500
Hausen [14]	$Nu_m = 3.66 + \frac{0.0668}{x^{*1/3}(0.04 + x^{*2/3})}$ $Nu = 0.037(Re^{0.75} - 180)Pr^{0.42}\left[1 + \left(\frac{D}{x}\right)^{2/3}\right]\left(\frac{\mu_m}{\mu_w}\right)^{0.14}$	Thermal entry, fully developed laminar flow, transitional flow Transition, thermal entry and fully developed turbulent flow	Empirical	$0 < x^* < \infty$ $10^4<Re<10^5$	 0.6-1000
Ghajar and Tam [12]	$Nu_l = 1.24\left[\frac{RePr}{x/D} + 0.024(GrPr)^{0.75}\right]\left(\frac{\mu_m}{\mu_w}\right)$ $Nu_{tr} = Nu_l + [\exp\left(\frac{a - Re}{b}\right) + Nu_t^c]^c$ $a = 1766, b = 276, \; c = -0.955$ $a = 2617, b = 207, \; c = -0.950$ $a = 6628, b = 237, \; c = -0.980$ $Nu_t = 0.023Re^{0.8}Pr^{0.385}\left(\frac{x}{D}\right)^{-0.0054}(\frac{\mu_m}{\mu_w})^{0.14}$	Laminar flow, combined entry and fully developed, $3 \le x/D \le 192$ Laminar fully developed, transition, combined entry, and fully developed turbulent flow, forced and mixed convection (Re-entrant enlet) , $3 \le x/D \le 192$ (Square-edged enlet), $3 \le x/D \le 192$ (Bell-mouth enlet), $3 \le x/D \le 192$ Turbulent combined entry and fully developed turbulent flow, forced convection, $3 \le x/D \le 192$	Empirical	$280 \le Re \le 3800$ 1,700<Re<9,100 1,600<Re<10,700 3,300<Re<11,100 7,000<Re<49,000	40-160 5-51 5-55 13-77 4-34

Table 2.2: Applicability conditions of the available correlations for heat transfer coefficients

Author	Forced convection	Laminar flow	Turbulent flow	Fully developed	Thermal Entry	Combined Entry	Transition flow	Mixed convection	Inlet geometry effect
Deissler [10]	✓		✓			✓			
Sieder and Tate [35]	✓	✓	✓	✓		✓			
Churchill-1 [9]	✓	✓	✓	✓			✓		
Churchill-2 [9]	✓		✓	✓					
Hausen [20]	✓	✓	✓	✓	✓		✓		
Gnielinski-1 [17]	✓		✓			✓	✓		
Gnielinski-2 [17]	✓		✓	✓			✓		
Gnielinski-3 [17]	✓		✓	✓			✓		
Mills [29]	✓		✓	✓		✓			✓
Molki and Sparrow [30]	✓		✓	✓		✓			
Al-Arabi [2]					✓	✓			
Ghajar and Tam-1 [14]	✓	✓		✓		✓	✓	✓	✓
Ghajar and Tam-2 [14]	✓	✓	✓	✓		✓	✓	✓	✓
Ghajar and Tam-3 [14]	✓		✓	✓		✓	✓	✓	✓

CHAPTER 3

EXPERIMENTAL SETUP AND METHODOLOGY

3.1   Overview

As stated in section 2.7, the objective of this research is to develop correlations to calculate heat

transfer in pipes of sizes $0 < L/D \leq 6$ and Reynolds numbers between 2,900 and 50,000. The

research is motivated by the need to accurately predict heat transfer in systems where the flow

is in the transitional and low Reynolds number turbulent flow regimes, and non-fully developed

due to relatively short pipe lengths. The objectives of this chapter are to:

1) Quantify the uncertainty in the experimental measurements,

2) Provide detailed descriptions of the setup and experimental methodology,

3) Demonstrate how the experimental conditions (e.g., target Reynolds numbers, non-fully

    developed flow) were achieved, and

4) Describe the experimental matrix.

3.2   Experimental Error Analysis

Experimental errors may be introduced during calibration, data acquisition, and data reduction.

During measurements both precision and bias errors might be present. The bias error is defined

as the average error in a series of repeated calibration measurements. Hence, the bias error is

the difference between the average and true value of the measured variable. Instruments were

zeroed prior to each measurement to minimize the probability of introducing bias errors.

Meanwhile, the precision error is the magnitude of the random variation of the repeated measurement, as shown in Figure 3.1 [28]. Each measurement was repeated at least three times to quantify the precision error.
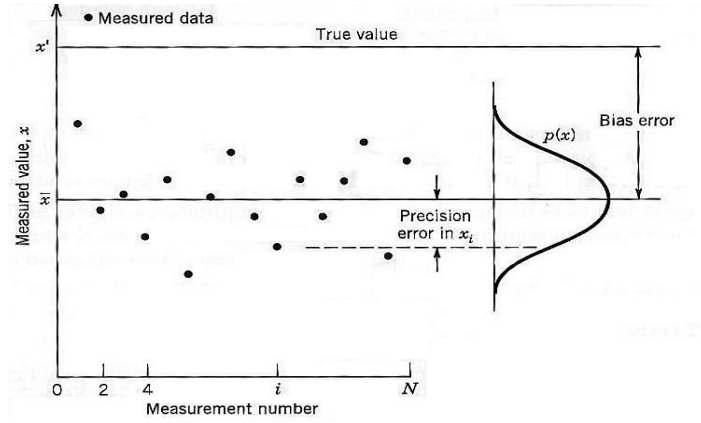
Figure 3.1: Distribution of errors of repeated measurements [28]

These were propagated according to equation 3.1. Results are shown in table 3.1 for each test parameter of interest.

$$u_R = \pm \sqrt{\sum_{i=1}^{L} (\theta_i u_{xi})^2} \qquad (3.1)$$

$R = f_1\{x_1, x_2, \ldots, x_L\}$

$u_R \equiv$ uncertainty propagation

$\theta_i \equiv$ sensitivity index

$u_{xi} \equiv$ contribution to the uncertainty

$x \equiv$ experimental variable

Table 3.1: Experimental uncertainty

Variable measured	Symbol	Equipment	Accuracy	Total error	Units
Voltage	V	MPJA 9903	0.5	0.5	mV
Current	I	DM-65 Multimeter	0.8% * FR+.5mV	0.6	mA
		Isotek CS-10	0.60		
Air Velocity	U	A/D converter quantization	0.1526	0.03	mV
		A/D converter quantization	0.0195		m/s
		TSI Alnor RVA801	0.02		m/s
Temperature	T	NI TB 9214	0.01	0.01	C
Length	L	Vernier	0.01	0.01	Mm
Convection heat transfer rate	Qc	-		0.01	W
Nusselt	Nu	-		1.83	-

3.3   Experimental Setup and Measurements

3.3.1   Experimental Setup

A schematic of the experimental setup is shown in Figure 3.2-a. From right-to-left, a wind tunnel, specifically designed and built for this research and described in more detail in section 3.2.2, generates the air flow. The air velocity can be varied by adjusting the input power to the blower. The heat tape was powered with a variable-voltage source, with voltage and current input ranges of 0-30 volts and 0-5 amperes, respectively and monitored to within 1 mV using digital multi-meters. Since the goal is for the supplied energy to transfer radially through the pipe and be carried out by convection, a five-millimeter layer of foam insulation was wrapped around the outer pipe wall to reduce heat transfer to the surroundings, as shown in Figure 3.3. For reference, the optimum insulation thickness was calculated from equation 3.2 [5] as 5.2 mm.

$$r_{cr} = \frac{k}{h} \tag{3.2}$$
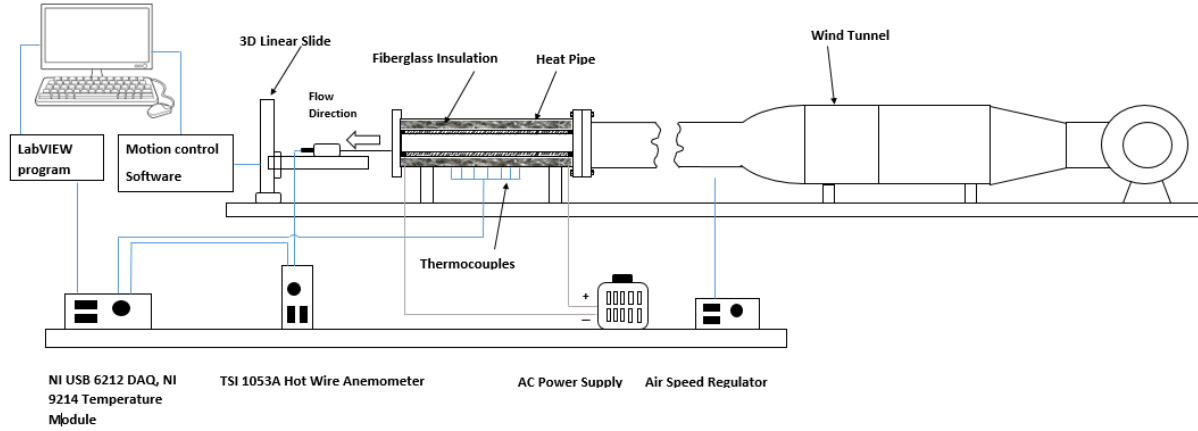
Figure 3.2-a: Schematic of the experimental setup for heat transfer and velocity measurements
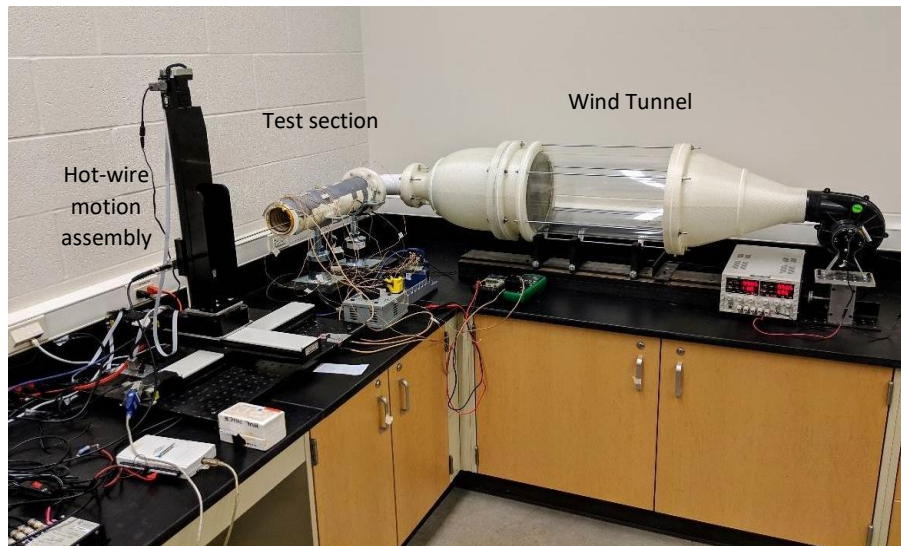
Figure 3.2-b: Experimental setup for heat transfer and velocity measurements, shown for the 90-degree entrance configuration

Figure 3.3: 3" diameter, 18" length foam insulated (acrylic pipe) test section

The air velocity was measured with a hot-film probe (TSI model 1750) mounted on a three-axis, motorized and computer-controlled translation stage. The computer program was developed in-house, as part of this research project.

Anemometer signals were collected through a data acquisition system (NI USB 6212), whereas thermocouple signals were gathered using an internally-compensated temperature module (NI 9214). A LabVIEW graphical user interface (GUI) was developed for system control and signal visualization. The experimental system is shown in Figure 3.2-b for one of the test configurations.

3.3.2   Wind Tunnel Development and Validation

A low-velocity wind tunnel Figure 3.4 was designed and built to generate uniform flow for Reynolds numbers between 2,900 and 50,000. Figures (3.4-a) and (3.4-b) show the wind-tunnel design and final product, respectively. The wind tunnel consists of a DC-powered air blower capable of generating a volume flow rate of up to 130 cubic feet per minute (221 m^3/h), a diffuser, a calming section incorporating a honeycomb structure, and a contraction.
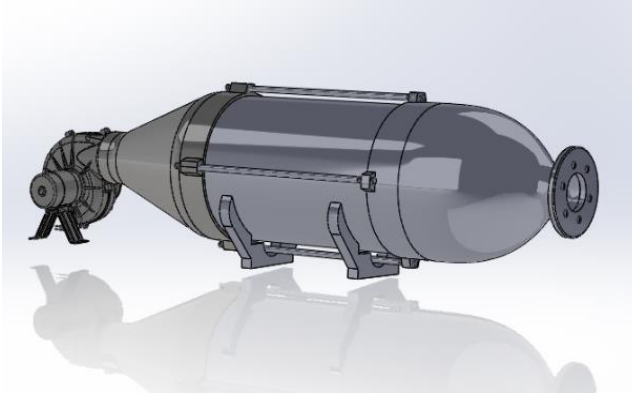
Figure 3.4-a: CAD wind tunnel design showing, from left to right: blower, diffuser, calming section and contraction
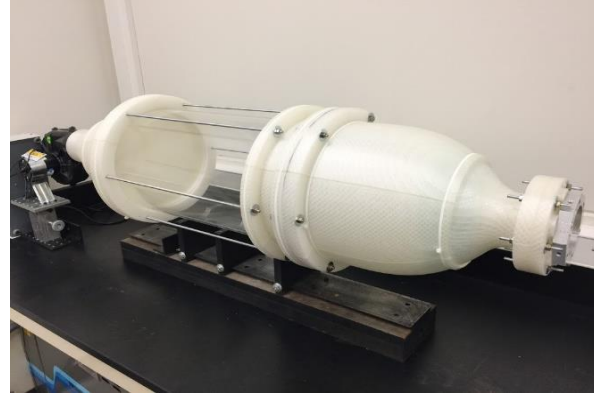
Figure 3.4-b:Final wind tunnel product
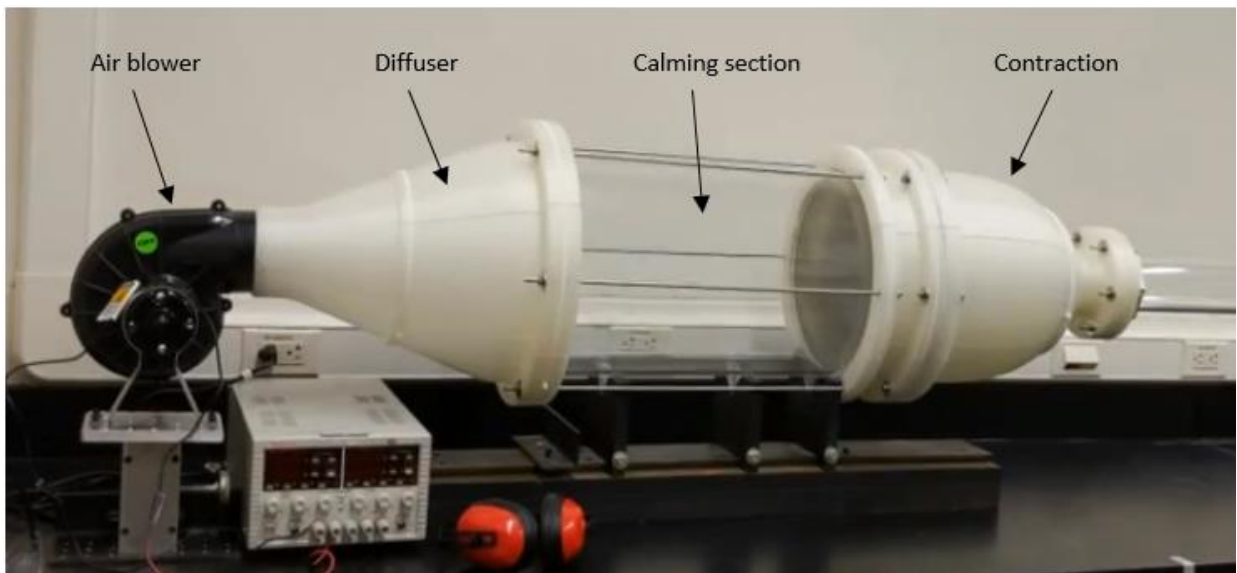
Figure 3.4-c: Wind tunnel components

After reviewing the design methods available in the literature ([43]-[46]), the two cubical method was adopted based on the need to develop flow uniformity at the wind-tunnel exit and prevent flow separation. Practical design considerations included the need to fit the wind tunnel and adjacent test sections in the available laboratory space (approximately 60 square feet), as well as material and machining costs.

Starting the design from the contraction component and using a three-inch intake diameter as a design constraint, a 4:1 contraction ratio was selected. Referring to Figure 3.5-a, for this

contraction ratio, the contraction length-to-inlet diameter ratio (L/D) was selected as one and

(x_m/L) was set to 0.75 (see Figure 3.5-b for terminology). The wall pressure coefficient (C_{pe}) at the

contraction exit, defined in equation 3.3, was less than 0.4 to avoid boundary layer separation

[43].

$$C_{pe} = 1 - (\frac{U_{2\infty}}{V_e})^2 \qquad (3.3)$$

Where:

$U_{2\infty} \equiv$ air velocity downstream the contraction exit.

$V_e \equiv$ velocity at the contraction exit

Then, the contraction profile was calculated using the two cubical equations 3.4, 3.5 [46]. Results

were imported to SolidWorks to create the 3-D design.

$$r_c = (R_1 - R_2)(1 - \left(\frac{x}{L}\right)^3 / \left(\frac{x_m}{L}\right)^2) + R_2, \quad x \le x_m \qquad (3.4)$$

$$\qquad (3.5)$$

$$r_c = (R_1 - R_2)\frac{(1 - \frac{x}{L})^3}{(1 - \frac{x_m}{L})^2} + R_2, \quad x > x_m$$
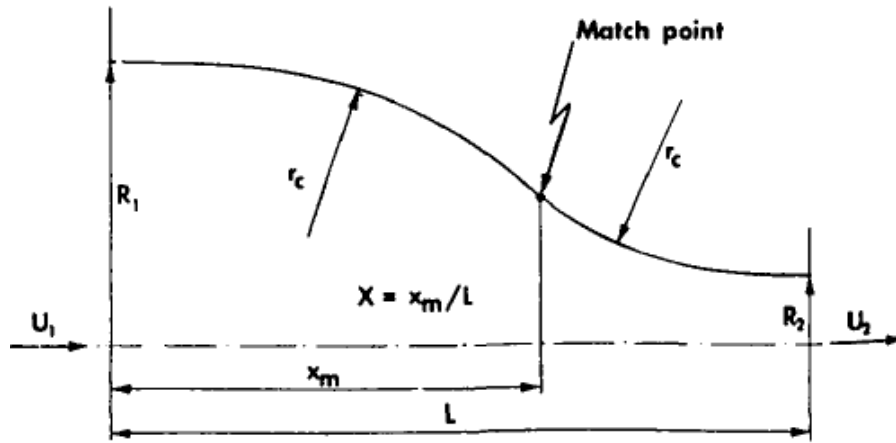
Figure 3.5-a: Contraction profile with two matched cubic arcs [43]

28
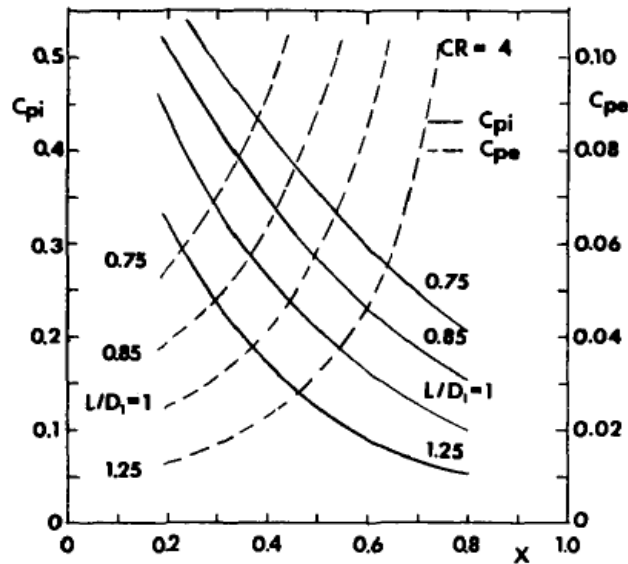
Figure 3.5-b: Design chart for a 4:1 contraction ratio (CR=4) [43]

To reduce the turbulence generated by the blower, a calming section consisting of a honeycomb structure in Figure 3.6 was implemented with two screens upstream the contraction. A bundle of five-millimeter diameter straws was cut in to 85 mm length and fitted inside an eleven-inch diameter acrylic cylinder between two 18x16 size screens. The diffuser was designed to smoothly adapt the flow between the four-inch blower exit and the eleven-inch acrylic cylinder. Technical drawings for all parts were generated using SolidWorks and exported for 3D printing at WMU's Machine Shop.

Once the wind tunnel was assembled, the flow velocity was measured at the exit to validate the flow uniformity and axisymmetry. The hot film anemometer probe was swept from left to right and back along the exit plane centerline in increments of 3 mm. Measurements were then repeated from top to bottom and back. At each location, 10,000 velocity measurements were taken and averaged.

Figure 3.6: Honeycomb structure

Results are shown in Figure 3.7-a for Re=50,000. The air exits at a uniform velocity of 9.00 m/s

with standard deviation of 0.03 m/s for the four tests mentioned above. The variation in velocity

was consistent with the probe error calculation (i.e., 0.03 m/s) discussed earlier in section 3.2

and presented in table 3.1. The overlap in the top-to-bottom and left-to-right profiles verify flow

axisymmetry.
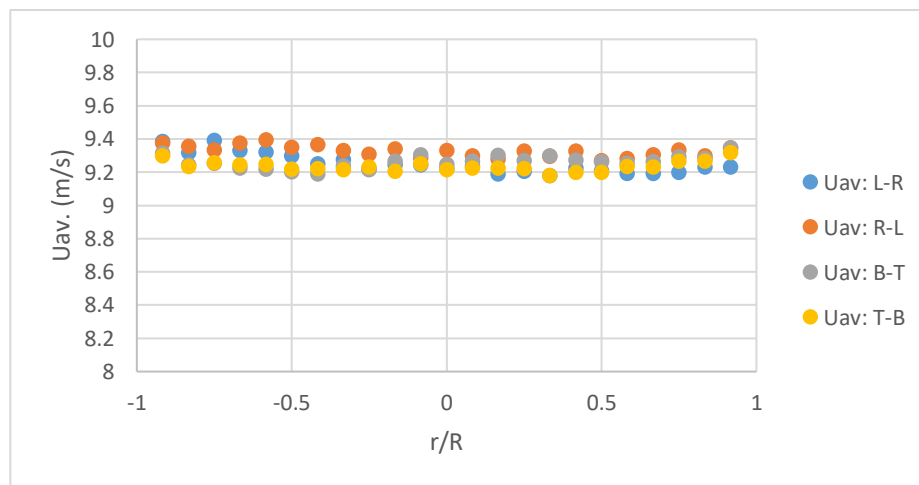
Figure 3.7-a: Velocity profiles at the wind tunnel exit, Reynolds 50,000. Left to right (L-R), right to left (R-L), top to bottom (T-B), and bottom to top (B-T)
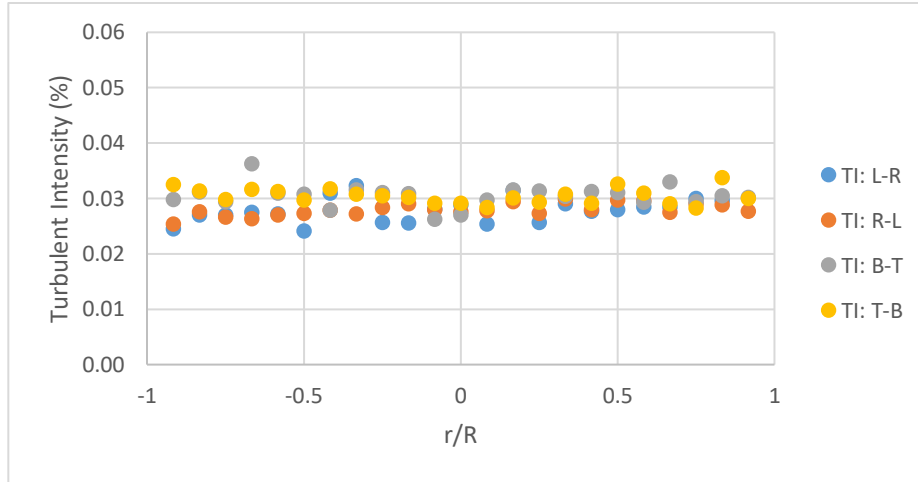
Figure 3.7-b: Turbulent intensity at the exit of the wind tunnel for Re=50,000

The corresponding turbulence intensity was calculated via equation 3.6 from the instantaneous velocity measurements at each location. As shown in Figure 3.7-b, turbulence intensities range between 2% and 4%.

$$\frac{\sqrt{\frac{1}{N}\sum_{i=1}^{N}(u')^2}}{\bar{u}} \qquad (3.6)$$

Where:

$u' \equiv$ instantaneous (turbulent) velocity

$\bar{u} \equiv$ mean velocity

Next, velocity profiles were measured to verify the presence of non-fully developed flows. Velocities were measured at locations (x/D) = 0, 6 and 48 at Re=50,000 without heating the pipe. Results, presented in Figure 3.8, show that at the wind tunnel exit (X/D=0) the velocity profile is uniform. Evidence of boundary layer development is seen farther downstream at X/D=6, which

is the target location for many of the measurements. Since the velocity profile is still changing between X/D=6 and X/D=48, it can be inferred that the flow is not fully developed at X/D=6.
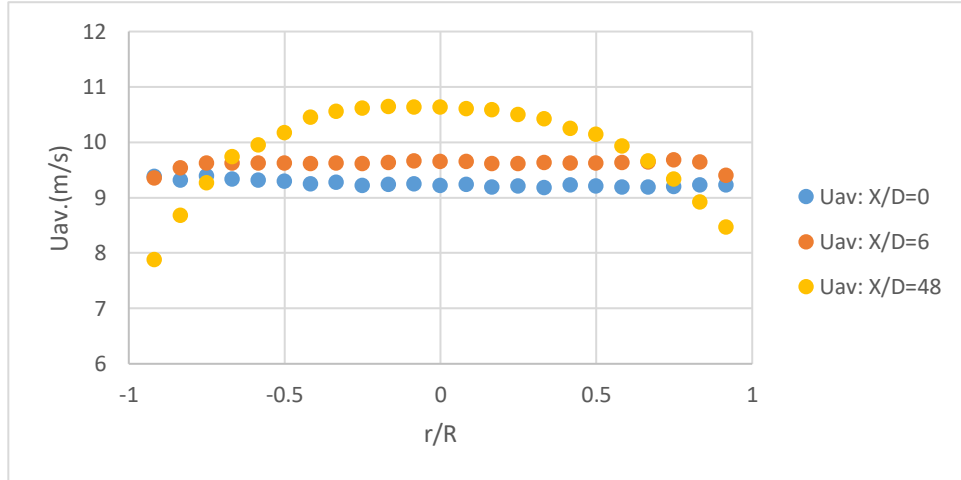
Figure 3.8: Velocity profile at x/D= 0,6 and 48

For reference, a wholly turbulent flow would be expected to achieve full development at 10<X/D<60 (i.e., between 2.5 ft and 15 ft for the current pipe diameter), whereas a laminar flow at Re~2000 and Pr = 0.7 would require approximately 18 ft to become fully developed.

3.4   Heat Transfer Measurements

The energy balance equation 3.7, schematically shown in Figure 3.9-a was used to quantify the convection heat transfer inside a circular tube. This method was replicated experimentally, as shown in Figure 3.9-b. The input electrical power to the heating tape (IV) is converted to a uniform radial heat flux that dissipates in three directions: convection heat transfer carried out by the air flow inside the tube, conduction through the insulation to the surrounding air, and radiation from external surfaces to the room walls. The thermocouple layout is shown in Figure

3.10. Equation 3.8 [5] was used to calculate heat losses from the ends of the pipe through the insulation by conduction in the axial direction.
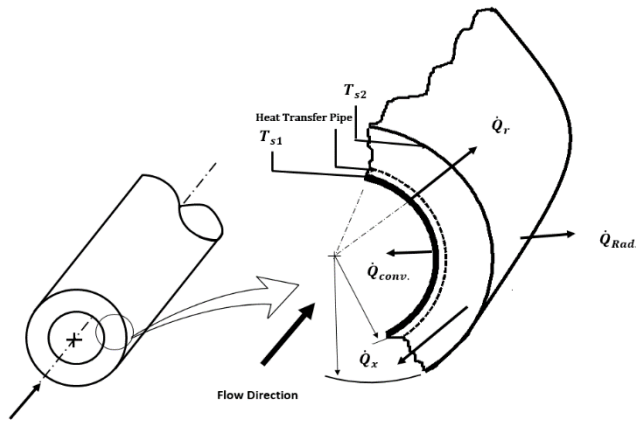
Figure 3.9-a: Energy balance method
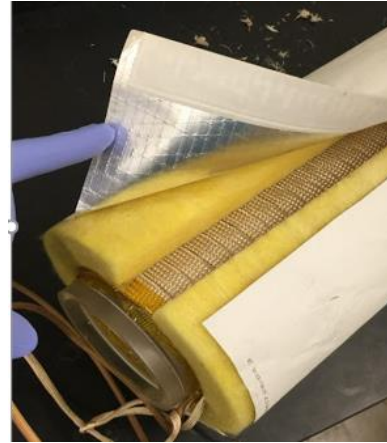
Figure 3.9-b: Actual test section

$$\dot{Q}_{conv.} = IV - (\dot{Q}_{cond} + \dot{Q}_{rad.})\qquad (3.7)$$

I= electric heating current, V= voltage across the heat pipe.
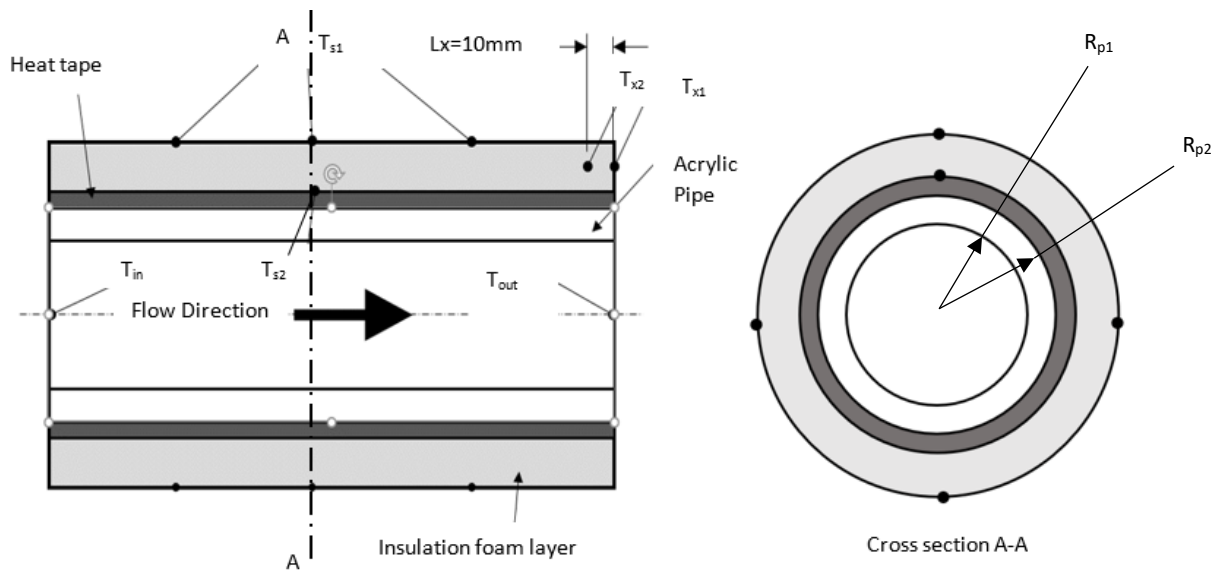
Figure 3.10: Thermocouple layout

$$\dot{Q}_x = \frac{k_{ins}A(T_{x1} - T_{x2})}{\mathrm{L}_x} \tag{3.8}$$

Where,

$k \equiv$ thermal conductivity of the insulation

$A \equiv$ insulation cross sectional area normal to the axial direction

$T_{s1}, T_{s2} \equiv$ inner and outer surface temperatures of the insulation, respectively

$L \equiv$ insulation length in the axial direction

The radial heat loss by conduction through the insulation was quantified using equation 3.9 [21]

using the values shown in table 3.2,

$$\dot{Q}_r = \frac{2\pi L k_p (T_{s1} - T_{s2})}{\dfrac{1}{h_c 2\pi r_1 L} + \ln\left(\dfrac{r_{p1}}{r_{p2}}\right)} \tag{3.9}$$

$r_{p1} \equiv$ inner pipe diameter
$r_{p2} \equiv$ outer pipe diameter

Although radiation heat transfer was expected to be negligible, it was calculated from equation

3.10 [5].

$$\dot{Q}_{Rad1-2.} = \frac{\sigma(T_1^4 - T_2^4)}{\dfrac{1 - \varepsilon_1}{\varepsilon_1 A_1} + \dfrac{1}{A_1 F_{12}} + \dfrac{1 - \varepsilon_2}{\varepsilon_2 A_2}} \tag{3.10}$$

Where,

$\dot{Q}_{Rad1-2} \equiv$ net radiation exchange between the test section outer surface (the insulation) and the room walls

$A_1 \equiv$ surface area of the outer surface of the test section (the insulation)

$A_2 \equiv$ internal surrounding surface area (room walls surface area)

$\sigma \equiv$ Stefan-Boltzmann constant: 5.6×10^{-8} W/m^2. K^4

$\varepsilon_1 \equiv$ emissivity of the outer surface of the test section

$\varepsilon_2 \equiv$ emissivity of the surrounding surface area (room walls surface area)

$F_{12} \equiv$ view factor: fraction of the radiation leaving surface 1 intercepted by surface 2.

The average convection heat transfer coefficient h_c was calculated from equation 3.9 and the average Nusselt number was calculated from equation 3.11

$$\overline{Nu} = \frac{h_c D_{in}}{k} \qquad (3.11)$$

Where:

$D_{in} \equiv$ the inner pipe diameter

$k \equiv$ thermal conductivity of air

Constants and parameters used in the heat transfer calculations are listed in table 3.2. These, and the equations previously described, were incorporated into a MATLAB routine to automate the calculations.

Table 3.2: Experimental parameters and constants

Constant	Unit	Value	Description
r_1	mm	45.00	insulation outer diameter
r_2	mm	50.00	insulation inner diameter
r_{p1}	mm	38.00	pipe inlet diameter
r_{p2}	mm	44.00	pipe outlet diameter
L	mm	450.00	length of the test section 18"
L_x	mm	10.00	distance between T_{x1} and T_{x2} (figure 3.10)
K	W/m. K	0.030	air thermal conductivity
$k_{ins.}$	W/m. K	0.026	thermal conductivity of insulation
k_p	W/m. K	0.2	thermal conductivity of the acrylic pipe
ε	-	0.9	test section surface emissivity
σ	W/m². K⁴	5.6 e-8	Stefan-Boltzmann constant
F_{12}	-	1	radiation shape factor

3.4.1   Temperature Measurement

The temperature gradient through the insulation, as well as the inlet and outlet flow temperatures are necessary to estimate the heat dissipated by conduction, convection and radiation, as illustrated in Figure 3.9-a. To measure temperatures, the test section was instrumented with 16 K-type thermocouples, purchased with standard calibration, which were positioned around the length and circumference of the pipe. The thermocouples were attached to the inner and outer surface of the insulation along the pipe in the radial direction, and at the ends of the pipe in the axial direction (see Figure 3.10). The air temperature at the inlet and outlet of the test section were also measured. The maximum power input was determined by equipment limitations. Due to the relative low input power, significant axial gradients in the mean-flow temperature were not measured. A direct consequence of this (and perhaps a significant limitation of this work) is the absence of Prandtl number dependence in the Nusselt number correlations. Figure 3.11 shows the variation of Prandtl number with temperature for air [5].
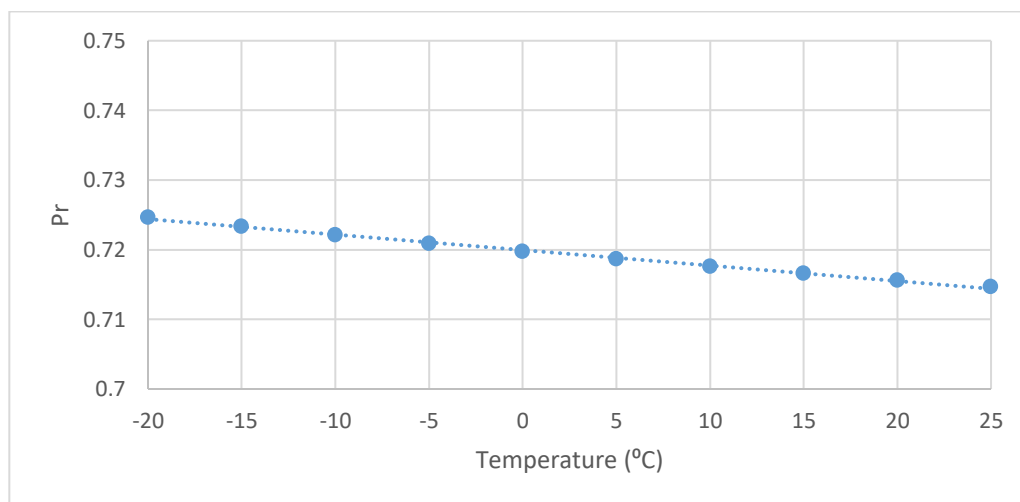

Figure 3.11: Variation of Pr for air with temperature

Between -20 °C and 25 °C, the Prandtl number changes within 1.4 percent. Since the axial temperature variation was less than 5°C, Prandtl number effects could not be taken into account in the development of the Nusselt number correlations. Heat transfer rates were calculated from the measured temperatures using the energy balance.

3.4.2 Velocity Measurement

Precise and accurate velocity and temperature measurements are required to develop heat transfer correlations. Since this investigation focuses on low Reynolds-number flows, traditional pitot tubes and pressure transducers are not accurate enough for velocity measurements. Instead, hot-wire (or film) anemometry was selected. This technique is well-suited for the present experiments because there are small concentrations of impurities in the flow, moderate turbulence intensities are expected, and the fluid and room temperatures are comparable, precluding the need for thermal compensation of the hot-film probe [25].

The constant temperature hot-film probe is an electric resistance connected to a Wheatstone bridge. When the probe is inserted into the flowing fluid, it cools down (mostly by convection), decreasing its resistance. The feedback circuit increases the heating current to maintain a constant probe temperature and rebalance the bridge. The voltage difference across the bridge is proportional to the flow velocity [25].

A hot-film anemometer mounted on computer- controlled, linear translation and rotary stages was used for experiments. Computer control was implemented to enable accurate angular adjustment and probe positioning in three-directions. The probe support width limited spatial resolution to one millimeter. The instantaneous velocity was recorded at 1 kHz over 10 seconds,

10 mm upstream the test section exit. These 10,000 samples were averaged to obtain a point-by-point average velocity and turbulence intensity.

3.4.3 Hot Wire Anemometer Setup

The following steps were followed to prepare the anemometer for first use once the physical connections were established:

1) The operating resistance was calculated using equation 3.12, based on the probe recommended operating temperature provided by the manufacturer, to maintain the desired temperature difference between the probe and the fluid around 250° C. Based on these calculations, a 47-ohm, 3-Watt operating resistance was integrated into the system.

$$R_H = R_o[1 + \alpha(t_h - t_o)] \qquad (3.12)$$

Where

$R_H \equiv$ resistance at operating temperature

$R_o \equiv$ resistance at ice point temperature

$\alpha \equiv$ temperature coefficient of resistance

2) The system response was optimized using the square-wave test. A LabVIEW function was developed to generate a 1 kHz input square-wave signal to the anemometer circuit. The output signal wave amplitude and time period were compared to the reference wave
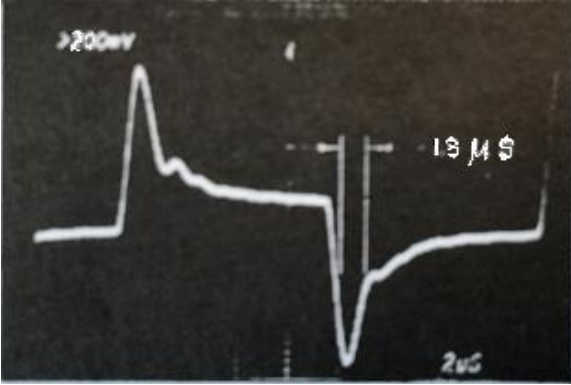
Figure 3.12-a: Standard output signal for TSI-10 hot film [25]
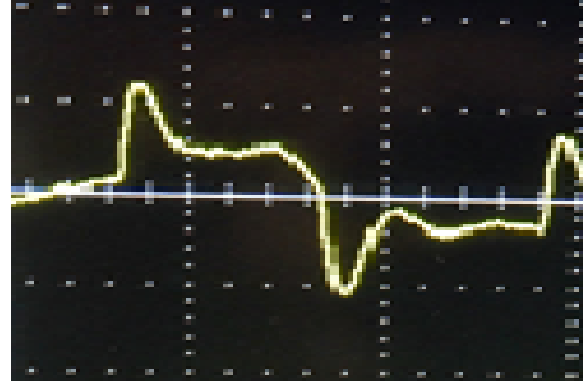
Figure 3.12-b: Experimental output signal captures with oscilloscope

provided with the anemometer for the hot film probe. Figure 3.12-a shows the standard output wave from the probe manufacturer [25], whereas Figure 3.12-b shows the output signal experimentally obtained. The captured wave shape in Figure 3.12-b was consistent with the reference signal.

3) Next, probe calibration methods were considered. Based on the target Reynolds numbers (2,900-50,000) and pipe geometry, velocities were anticipated between 0.25 m/s and 10 m/s. Since probe calibration at low velocities is challenging, various methods were explored, and multiple calibration experiments were conducted to obtain a reliable calibration curve:

a) Pressure transducers. A Kiel probe was located at the exit of the wind tunnel to measure the difference between the dynamic and static pressure generated by the flow. The pressure difference was converted to velocity using Bernoulli's Equation 3.13. These velocity values were correlated voltage signal from the hot film probe. The Kiel probe's accuracy decreased below 10 m/s. This can be seen in Figure 3.13, which shows calibration curves obtained with the Kiel probe and the tank discharge

method (discussed next). Due to the need to measure velocities below 10 m/s to target the required Reynolds numbers, the Kiel probe was not further considered.

$$U = \sqrt{2\frac{\Delta P}{\rho}} \qquad (3.13)$$
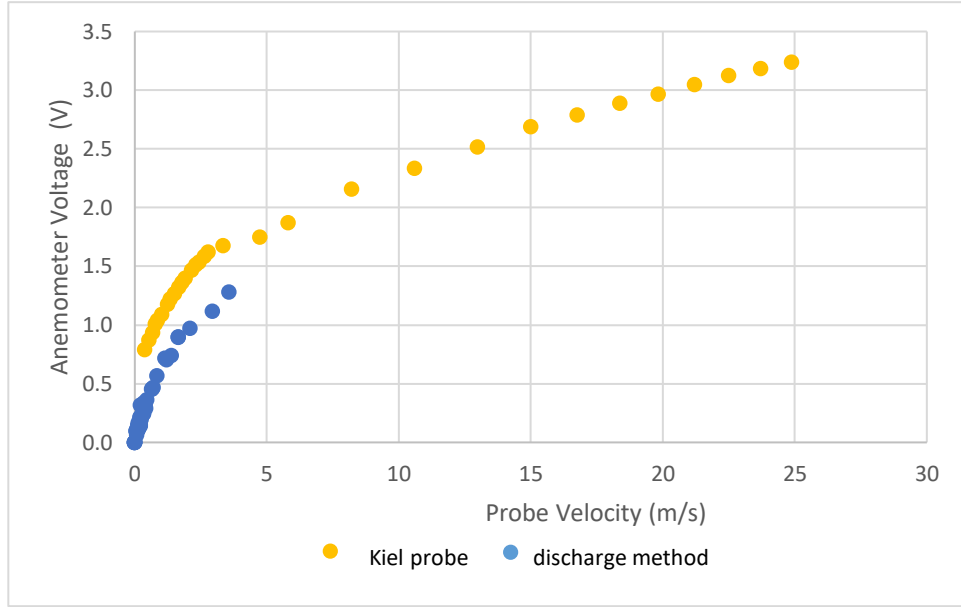
Figure 3.13: Calibration curve obtained with Kiel probe and tank discharged method

b) <u>Tank discharge method.</u> This method is schematically illustrated in Figure 3.14. When water drains from large tank, air flows at the same volume flowrate to occupy the tank vacancy. Since the water volume flowrate is directly proportional to the rate of change of the water level (dh/dt), the method can be used to estimate the intake air velocity [32]. That is, the water volume flowrate is calculated from dh/dt and the inlet velocity at D_1 is calculated using equation 3.14, assuming incompressible flow.
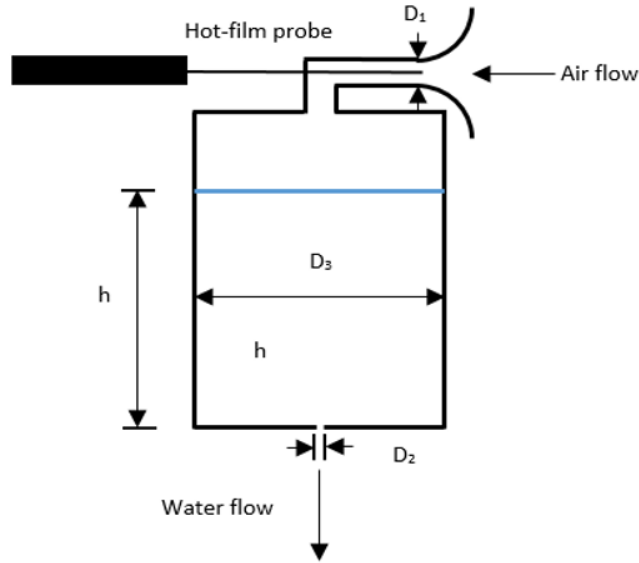
Figure 3.14: Tank discharged method for low velocity calibration

$$U_1 D_1^2 = D_2^2 \frac{dh}{dt} \qquad\qquad (3.14)$$

c) <u>Rotating vane anemometer.</u> A rotating vane anemometer (TSI Alnor RVA801), shown in Figure 3.15, was used to measure the air velocity directly for hot film probe calibration. The vane anemometer specifications are provided in Appendix (B-5). The most desirable features were its improved detectability: 0.2 m/s, which was favorable at low Reynolds numbers, and accuracy: 0.02 m/s. Velocity values obtained with the vane anemometer between 0.2 m/s and 10 m/s were correlated to hot film probe voltages captured at the same location.

Calibration data are shown in Figure 3.16-a for the vane-meter method. Both the discharge and vane meter methods proved to be repeatable for required velocity range (0.2 m/s -10 m/s). However, the vane-meter method was selected because it was more convenient, and easier to use. Figure 3.16-b shows the vane-meter calibration, the x-axis

represents the wind tunnel voltage (used to regulate the velocity) and the y-axis shows the vane-meter velocity measurements. The velocity data from the vane-meter was correlated with hot-film probe voltage at the same location and same wind tunnel voltage increments.

Figure 3.15: Vane meter used for hot film probe calibration
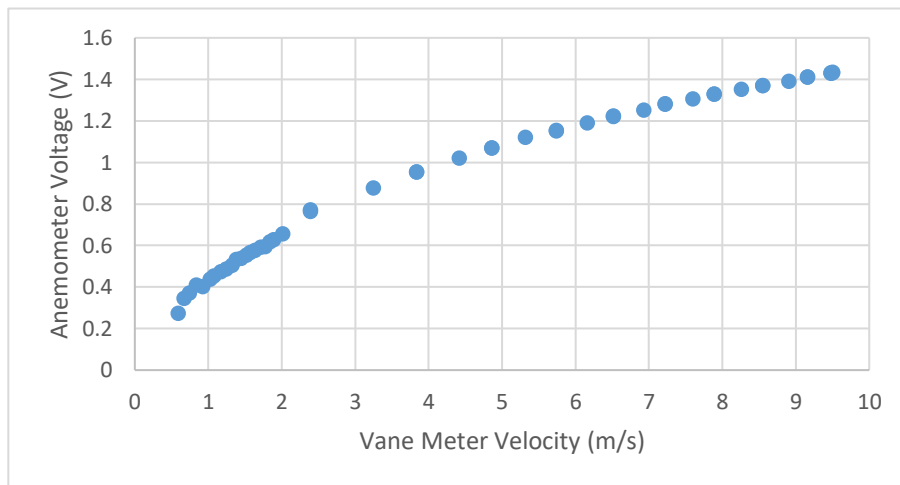
Figure 3.16-a: TSI vane meter calibration curve
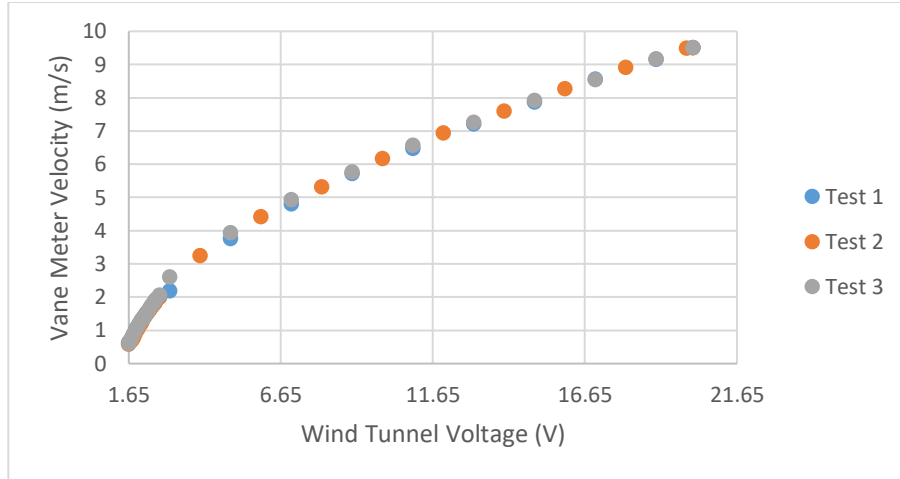
Figure 3.16-b: TSI vane meter calibration versus wind tunnel voltage

3.5 Experimental Matrix and Non-Dimensional Groups

As shown in Figure 3.17, the experimental work was divided in three phases based on the entrance geometric configuration: uniform, tripped flow and 90-degree. For all, combined entry conditions (i.e., where both hydrodynamic and thermal boundary layers are developing simultaneously) with uniform heat flux were imposed.

- **Phase I: Uniform Flow.** For this phase, the test section was connected horizontally and directly to the exit of the wind tunnel. Flow uniformity was discussed in section 3.2.2, Figure 3.7. The heat transfer was quantified for four Reynolds numbers: 2,900, 10,000, 30,000, and 50,000, as shown in table 3.3. During each test, the surface temperatures were monitored until no change with time was detected. At this point the system was considered at steady state. Then, ten temperature readings were recorded for each thermocouple. The temperature data were then averaged, and the heat transfer was calculated using the MATLAB routine developed for this project.
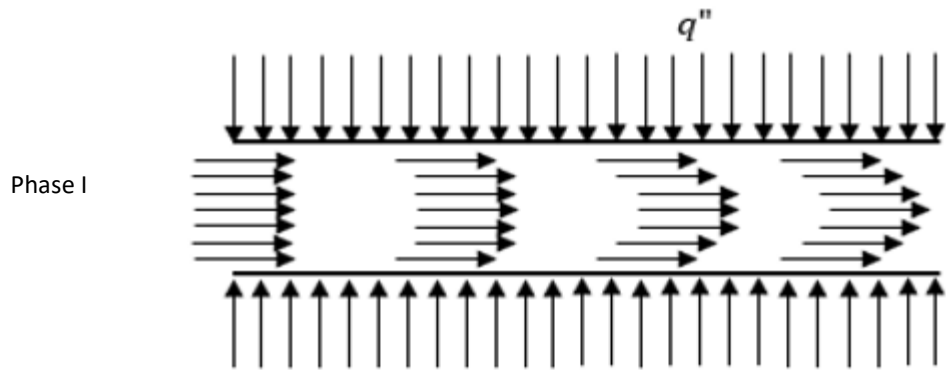
Figure (3.17-a):

Combined, uniform flow entry
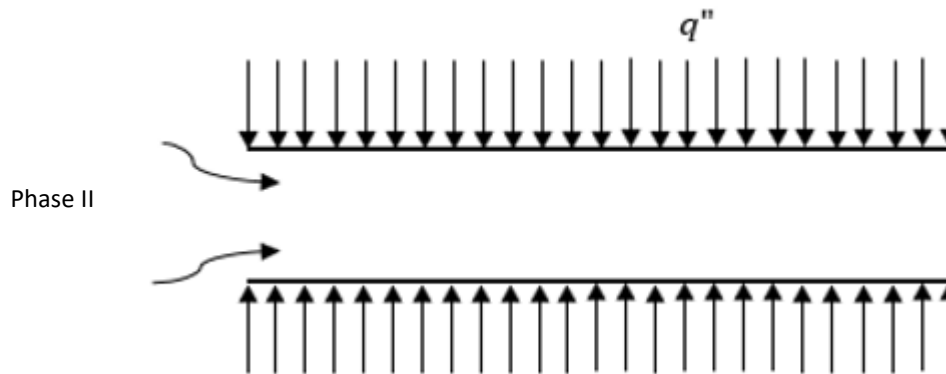
Phase I

Figure (3.17-b):

Combined, tripped flow entry
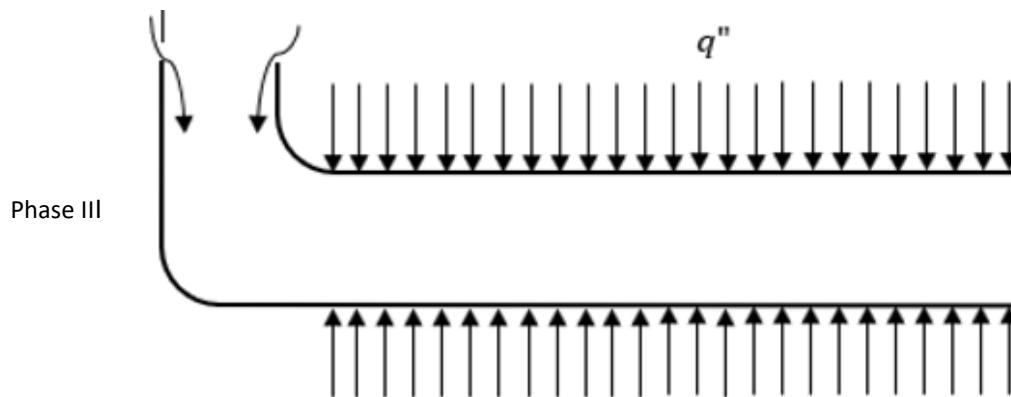
Phase II

Figure (3.17-c):

Combined, 90-degree entry

Phase III

- **Phase II: Tripped Flow.** The plate shown in Figure 3.18 was clamped between the wind tunnel exit and the test section to generate turbulence. The opening dimensions are (20 mm x 75mm), coincident with the wind tunnel centerline. Experiments were conducted as described in Phase 1.
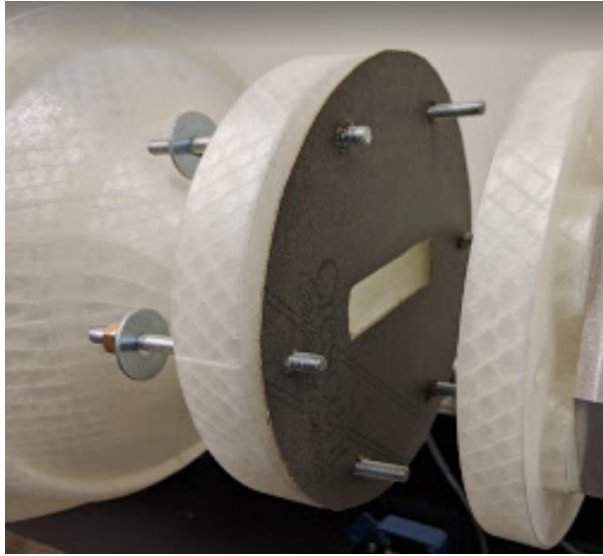
Figure 3.18: Turbulence generator plate

- **Phase III: Ninety-Degree Entrance.** A three-inch diameter, PVC, 90° elbow Figure 3.19 was

  attached to two designed and 3D-printed flanges and connected between the exit of the

  wind tunnel and the test section to divert the flow perpendicular to the wind tunnel exit.

  Experiments were conducted as described in Phases 1 and 2. Table 3.3 summarizes

  measured variables, targeted outputs and dimensionless parameters.

Figure 3.19: Three-inch diameter, PVC, 90° elbow

Table 3.3: Experimental matrix

Experiment Type	Exp .#	Re	x/D	U mean (m/s) ± 0.03	Probe direction	Mean flow Temp. (°C) ± 0.01	Voltage (V) ± 0.5 mV	I (A) ± 0.5 mA	Objective
Wind tunnel validation and flow characterization	1	50,000	0	9.60	Left-right	24.00	0.0000	0.0000	Flow uniformity, axisymmetry
	2	50,000	0	9.60	Right-left	24.00	0.0000	0.0000	
	3	50,000	0	9.60	Top-bottom	24.00	0.0000	0.0000	
	4	50,000	0	9.60	Bottom- top	24.00	0.0000	0.0000	
Phase I uniform flow entry	1	2,800	6	0.27	Left-right	24.84	16.6500	0.4000	Nusselt number
	2	10,000	6	2.50	Left-right	24.16	16.6500	0.4000	
	3	30,000	6	7.60	Left-right	24.72	16.6500	0.4000	
	4	50,000	6	9.70	Left-right	25.09	16.6500	0.4000	
Phase II tripped flow entry	1	2,800	6	0.27	Left-right	26.45	16.6500	0.4000	Nusselt number
	2	10,000	6	2.50	Left-right	25.71	16.6500	0.4000	
	3	30,000	6	7.60	Left-right	26.29	16.6500	0.4000	
	4	50,000	6	9.70	Left-right	26.85	16.6500	0.4000	
Phase III 90-degree entry	1	2,800	6	0.27	Left-right	27.64	16.6500	0.4000	Nusselt number
	2	10,000	6	2.50	Left-right	25.73	16.6500	0.4000	
	3	30,000	6	7.60	Left-right	25.39	16.6500	0.4000	
	4	50,000	6	9.70	Left-right	26.40	16.6500	0.4000	

CHAPTER 4

RESULTS AND DISCUSSION

4.1 Overview

In this chapter, non-dimensional heat transfer results are presented and discussed for the three experimental configurations: uniform, tripped, and 90-degree entrance. All results correspond to combined entry and uniform heat flux conditions for Reynolds numbers between 2,900 and 50,000. Current results are also compared to available data in the technical literature.

4.2 Velocity Profile and Turbulence Intensity

Figures 4.1, 4.3, and 4.5 shows mean velocity profiles for uniform, tripped, and 90-degree entry conditions at four Reynolds numbers: 2,800, 10,000, 30,000, and 50,000, ten millimeters upstream the heated test section exit at X/D=6. As expected, Reynolds numbers increase with increasing velocities. The decrease in the velocity values near the walls is also expected due to viscosity effects. Mean velocity profiles for the uniform entry condition remain fairly consistent at all Reynolds numbers, while clearly the tripping orifice and 90-degree elbow introduce disturbances into the mean flow that carry over to X/D=6. Figure 4.2 shows the turbulence intensity for the same Reynolds number range normalized by the mean centerline velocity. Results reveal higher *normalized* turbulence intensity at the Reynolds numbers. Figure 4.3 shows the mean velocity profile for the tripped-flow entry. Since the flow was tripped and the boundary layer was regenerated, the velocity profile is no longer uniform. The turbulence intensity for the

tripped-flow, shown in Figure 4.4, is consistently higher and less spatially uniform than for the uniform entry condition (shown in Figure 4.2).

The mean velocity profile for the 90-degree entry condition, shown in Figure 4.5, is higher in magnitude and no longer axisymmetric, as the flow accelerates on the left side of the bend (see Figure 4.5). The corresponding turbulence intensity is shown in Figure 4.6. It can be noticed that the turbulence intensity is affected by the velocity change around the bend, resulting in a normalized lower value at the higher mean-velocity side.

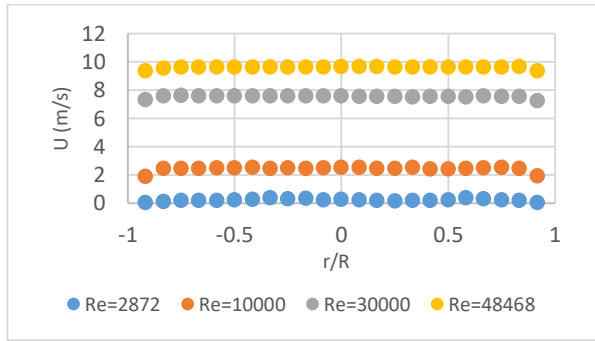*Figure 4.2: Velocity profile for uniform flow entry (x/D=6)*
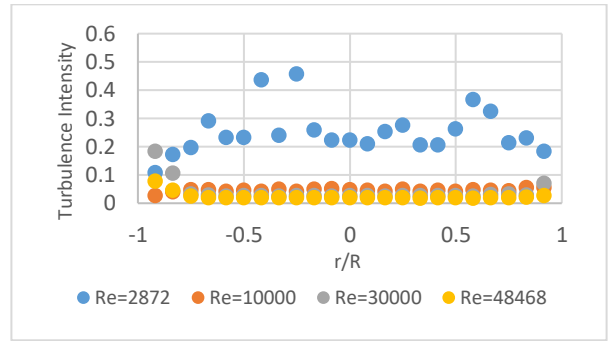
Figure 4.3: Turbulence intensity, uniform flow entry(x/D=6)
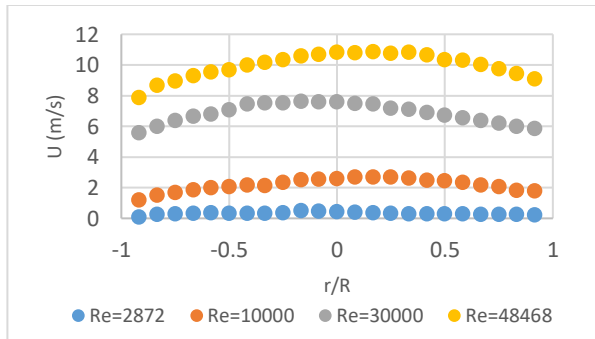
Figure 4.3: Velocity profile for tripped flow entry (x/D=6)
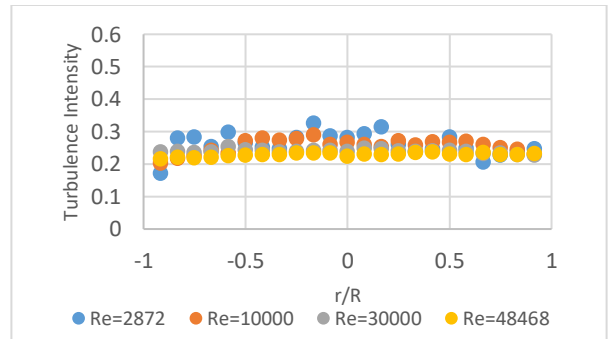
Figure 4.4: Turbulent intensity, tripped flow entry(x/D=6)
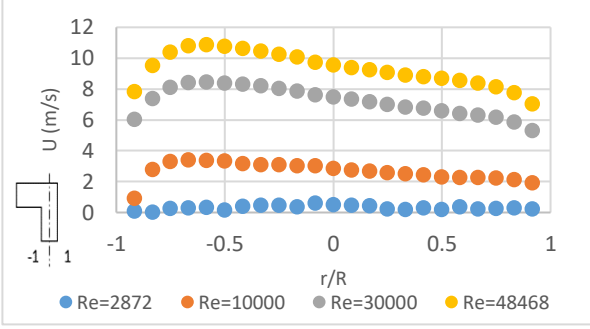
Figure 4.5: Velocity profile for 90-degree entry (x/D=6)
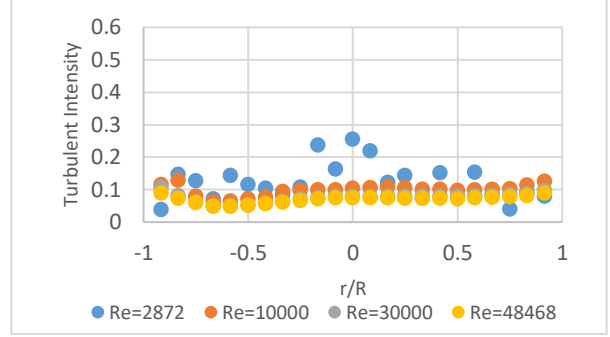
Figure 4.6: Turbulence intensity, 90-degree entry (x/D=6)
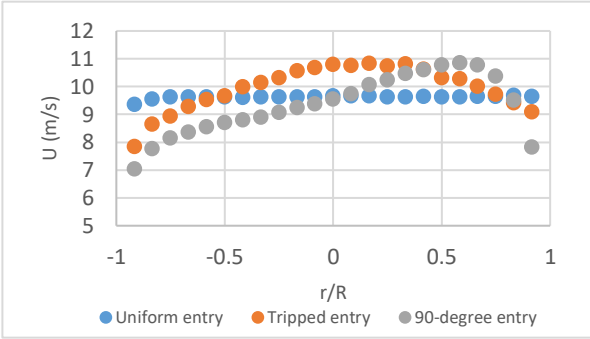
Figure 4.7: Velocity profile for different entry conditions, Re=50,000, (x/D=6)
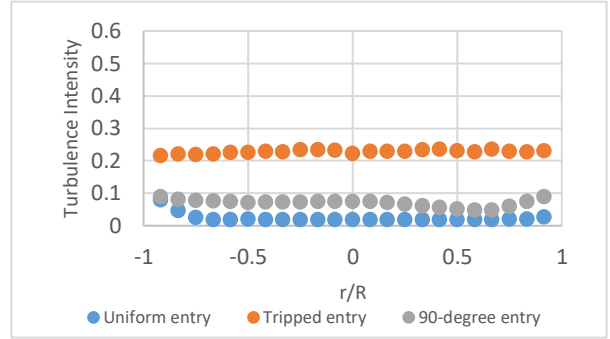
Figure 4.8: Turbulence intensity for different entry conditions (x/D=6), Re=50,000

Figure 4.7 shows mean velocity profiles for the three different entry conditions at Re=50,000. The turbulence intensity is compared in Figure 4.8 for the same Reynolds number. The tripped flow exhibits higher turbulence intensity, which is expected due to secondary flows created by the tripping orifice.

4.3 Heat Transfer Results

Equations 3.7 through 3.9, presented in section 3.4, were used to quantify heat transfer rates from conduction (axial and radial), radiation, and convection for input power values of 6.7 W, 10.4 W, and 15 W.

A schematic of the test section is reproduced in Figure 4.9 for convenience. Notice that four thermocouples were located around the pipe circumference with 90 degree spacing. As shown

in Figure 4.10, at steady state, all values were within 1° C of each other; therefore location 1 was used to calculate the heat transfer rate.

Heat transfer rate results are shown in table 4.1. Values in parentheses represented percentages of the input power. It is apparent that heat transfer by axial conduction and radiation are negligible, whereas convection is the dominant heat transfer mechanism and is also relatively insensitive to the input power over the range considered.
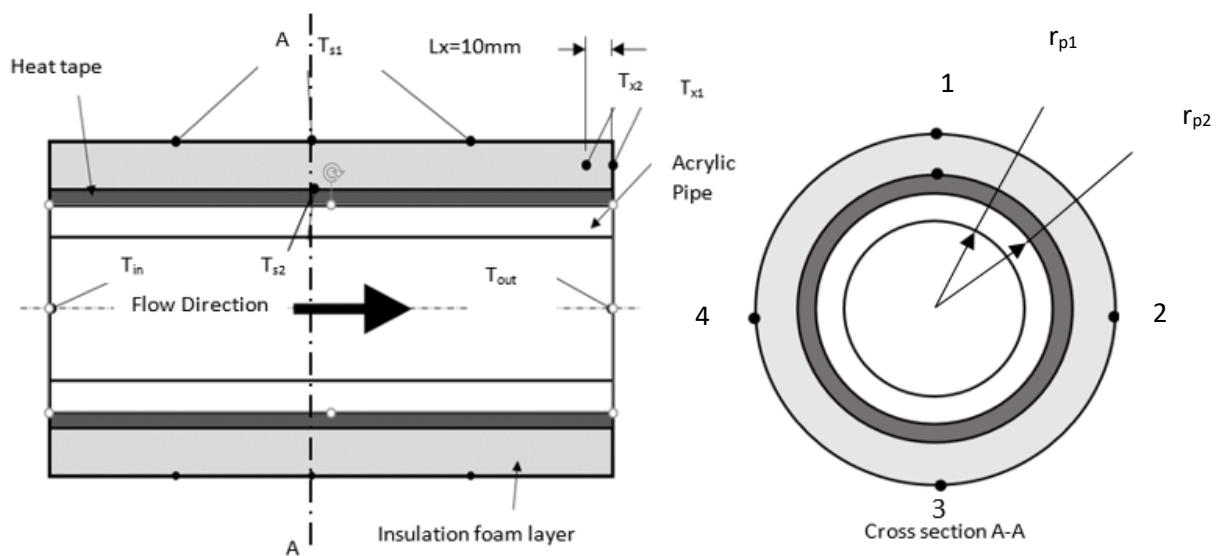
Figure 4.9: Thermocouple layout
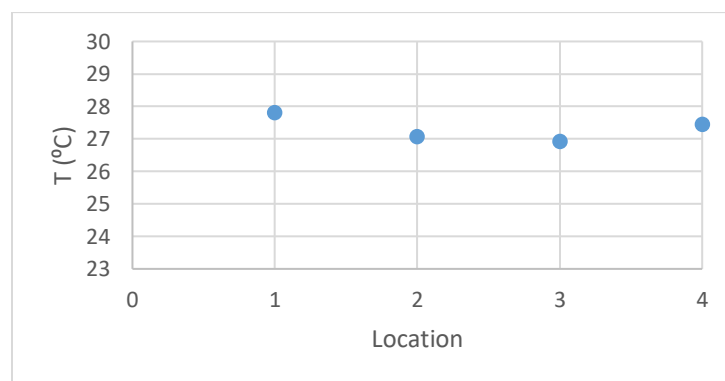
Figure 4.10: Circumferential temperature distribution

Table 4.1: Heat losses by convection, conduction and radiation. Values in parenthesis represent the percentage of power input

Power (W)	Convection heat loss (W)	Radial Conduction heat loss (W)	Axial conduction heat loss (W)	Radiation heat loss (W)
6.71	5.26 (78%)	1.45 (22%)	4.22×10^{-6}	0.0018
10.41	8.41 (81%)	1.99 (19%)	3.52×10^{-6}	0.0017
15.38	12.57 (82%)	2.81 (18%)	3.80×10^{-6}	0.0024

Best-fit curves were applied to the experimental data for the uniform, tripped, and 90-degree entry conditions. Results are given by equations 4.4 through 4.6. These correlations are presented in Figures 4.11 through 4.14. Best-fit curves are also shown on the graphs.

$$Nu = 0.099 Re^{0.582} \tag{4.4}$$

$$Nu = 0.174 Re^{0.576} \tag{4.5}$$

$$Nu = 0.0617 Re^{0.652} \tag{4.6}$$

While the overall trend of increasing Nusselt numbers as the Reynolds number increases is consistent for all entrance configurations, Nusselt number (and hence convection heat transfer magnitudes) differ for each case. This is more clearly displayed in Figure 4.14, where all entrance conditions are simultaneously shown. Clearly, Nusselt numbers are highest for tripped flow entry and lowest for uniform flow entry. This follows from turbulence effects: the honeycomb screens within the wind tunnel reduce the turbulence by damping large eddies, forcing the flow to become uniform prior to the wind tunnel exit. However, adding the tripping orifice regenerates the turbulence by creating secondary flows, which increase the Nusselt number. To further illustrate this point, Figure 4.15 shows the Nusselt number dependence on turbulence intensity

for uniform, tripped and 90-degree entry conditions at 10,000, 30,000, and 50,000 Reynolds numbers. As the turbulence intensity increases from uniform to tripped flow, the Nusselt number increases significantly. It is consistently shown in the technical literature that modifying the uniformity of the velocity profile using orifices, sharp edges, etc. increases the Nusselt number [19],[20],[15]. While the increase has been attributed to a turbulence enhancement, this work presents (to the author's knowledge) first evidence correlating the turbulence intensity to the Nusselt numbers for low-Reynolds number flows. The present trends were verified to apply under uniform heat flux and combined-entry conditions, noting that Prandtl number effects could not be quantified with the current experimental setup.
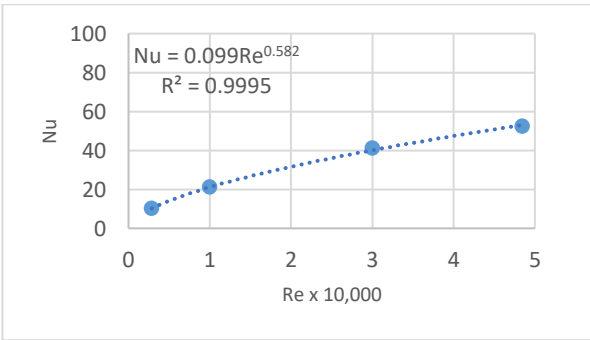
Figure 4.11: Heat transfer coefficient for uniform flow entry, Q=6.5 W
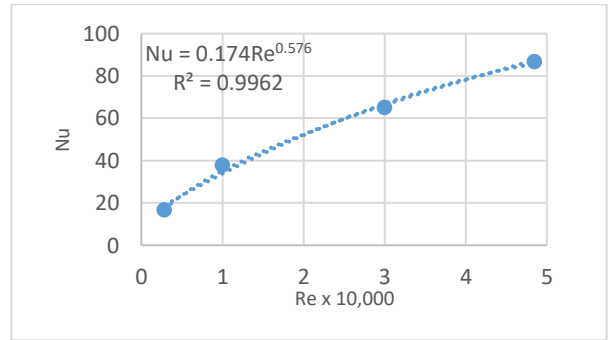
Figure 4.12: Heat transfer coefficient for tripped flow entry, Q=6.5 W
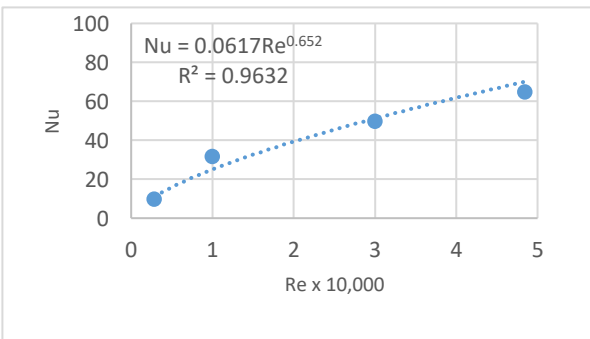
Figure 4.13: Heat transfer coefficient for 90-degree entry, Q=6.5 W
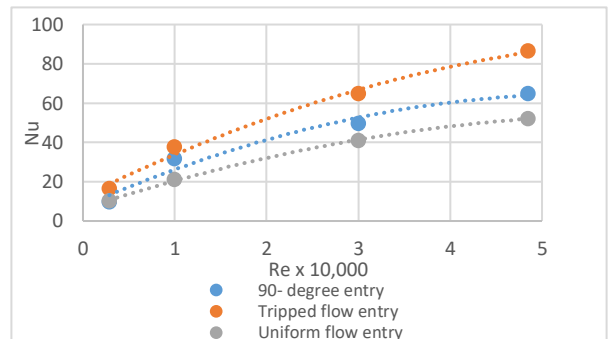
Figure 4.14: Heat transfer coefficient for various entry conditions
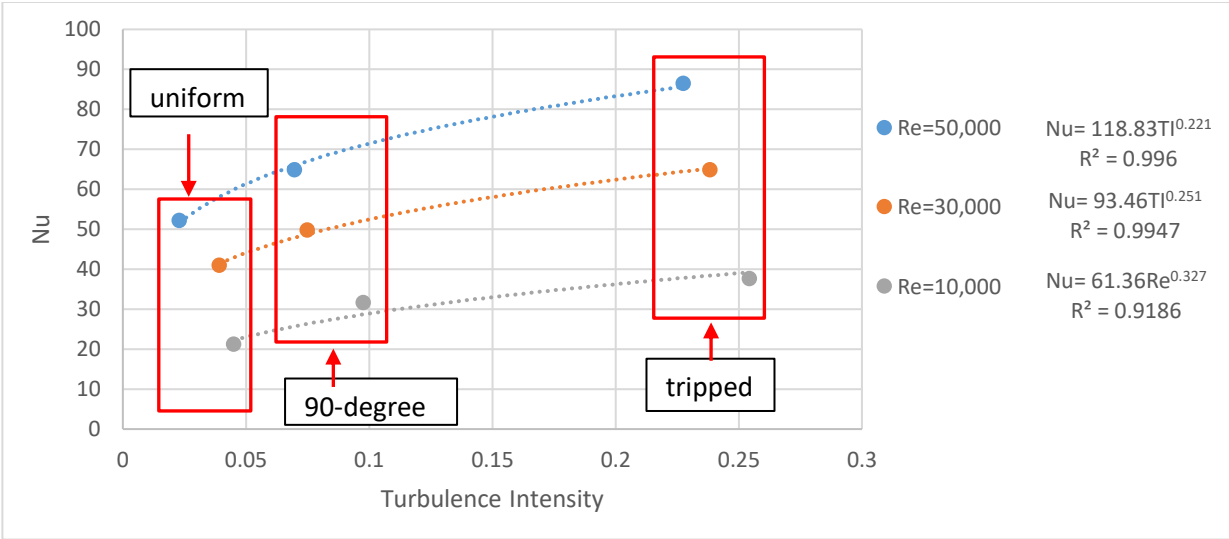
Figure 4.15: Heat transfer coefficient dependence on turbulence intensity for uniform, tripped and 90-degree entry, Re=50,000, Q=6.5 W

Next, Nusselt number data are compared to previous work of Colburn [5], Gnielinski [17], and Mills [49]. Table 4.2 lists the restrictions and range of applicability of the correlations used for comparison. Although Colburn's correlation applies to fully developed, turbulent flows, which clearly differs from the non-fully developed flow condition investigated in this work, it was selected as a reference correlation because it is widely known and often a default heat transfer correlation in simulation software. Based on the range of applicability shown in table 4.2, the present empirical correlation is expected to come closest to Gnielinski's, as both target low Reynolds number flows in combined entry. Notice however, that Gnielinski's correlation covers a broader Reynolds number range, reaching the wholly turbulent flow regime. Also, as previously discussed, Gnielinski's correlation was developed based on interpolation between available laminar and turbulent flow experimental data. The present correlation covers transitional flows between 2,900 < Re < 50,000 and was developed via direct measurements. Mills' and Colburn's correlation apply to fully-developed flows.

Table 4.2: Turbulent and transitional flow correlations

Author	Correlation	Conditions	Re	Pr
Colburn [5]	$Nu_D = 0.023Re_D^{4/5}Pr^{1/3}$ (4.1)	Turbulent fully developed	$10^4<Re<10^5$	0.6-160
Gnielinski [17]	$Nu = 0.0214(Re^{0.8} - 100)Pr^{0.4}$ (4.2)	Transition, turbulent combined entry	$10^4<Re<5\times10^6$	0.5-1.5
Mills [29]	$Nu = 0.0397Re^{0.73}Pr^{0.33}$ (4.3)	Turbulent flow, fully developed, uniform heat flux	$10^4<Re<10^5$	0.7

Results are shown in Figures 4.16 through 4.18. From Figure 4.16, the present correlation consistently predicts lower Nusselt numbers, although the discrepancy with the reference correlations decreases as the Reynolds number decreases.

As shown in Figure 4.17, the tripped flow, which exhibits the highest turbulence intensity of all entry conditions investigated, shows closer agreement with the reference correlations (e.g., Colburn's, Mills', and Gnielinski's). However, as discussed earlier, turbulence intensity variations between entry conditions have not been directly quantified and correlated to Nusselt numbers in the reference studies used here for comparison. It is possible that, if plotted as a function of turbulence intensity, the Nusselt numbers from previous studies would be in closer agreement to the current values.
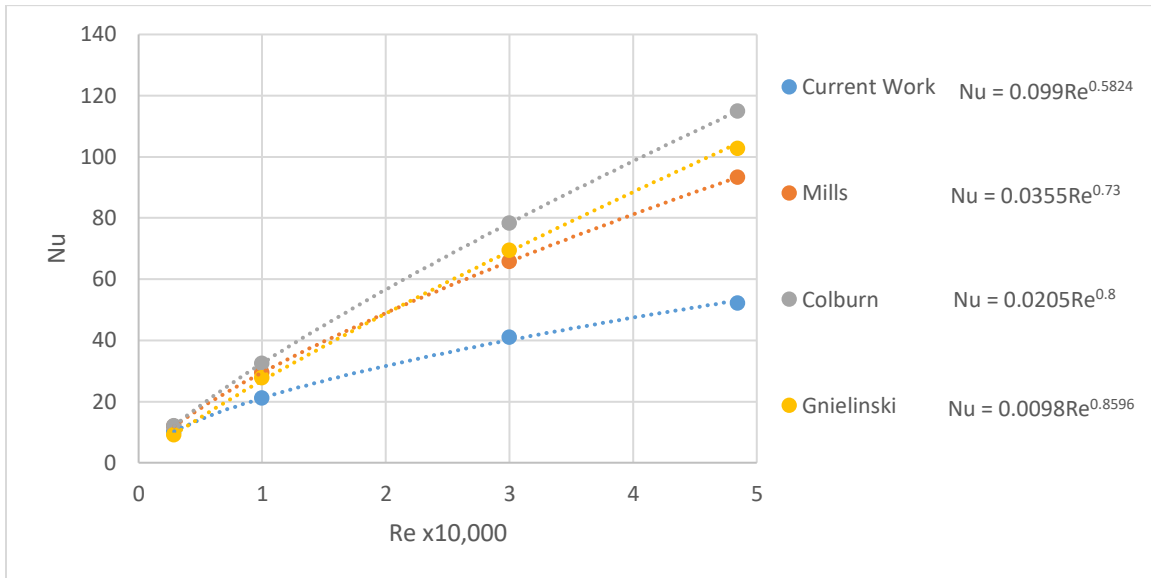
Figure 4.16: Heat transfer coefficient for current work (uniform flow entry) compared to reference correlations
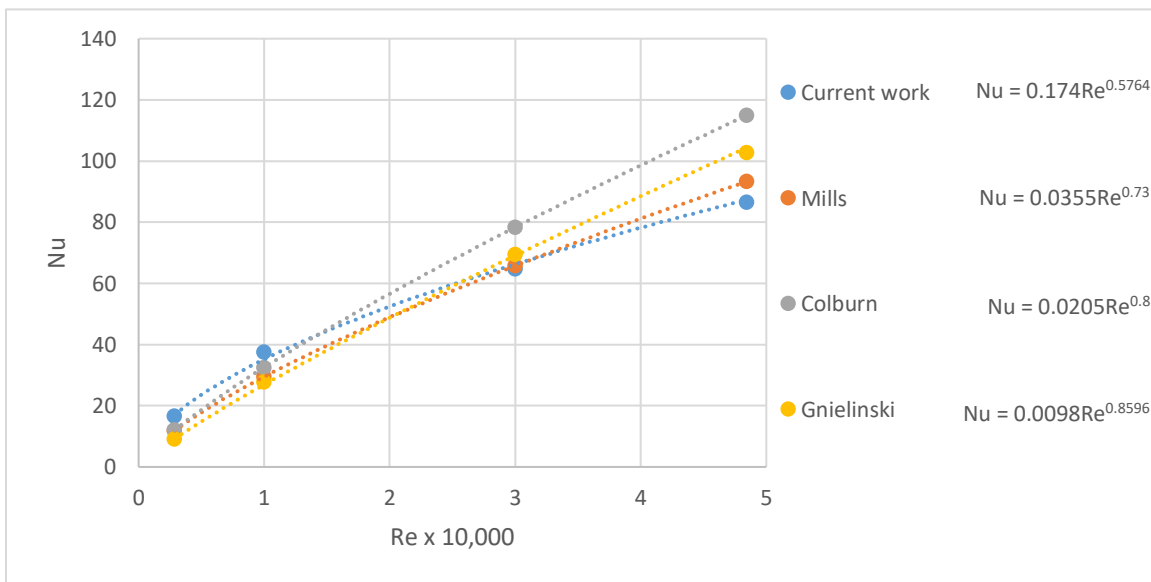
Figure 4.17: Heat transfer coefficient for current work (tripped flow entry) compared to reference correlations
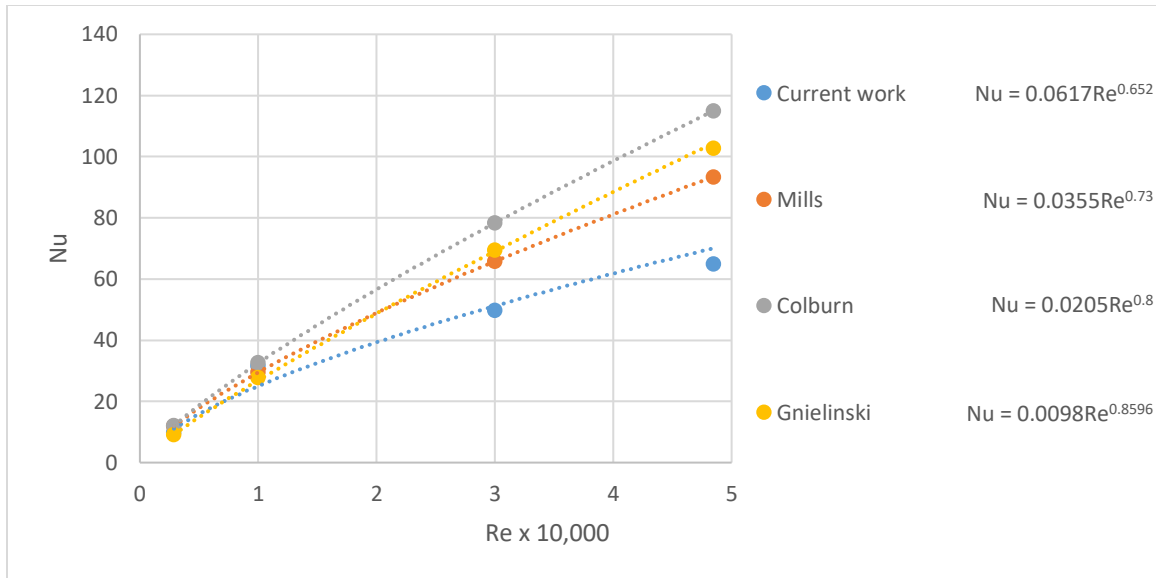
Figure 4.18: Heat transfer coefficient for current work 90-degree entry) compared to previous correlations

4.4 Practical Considerations

As described in Chapter 2, the main motivation for this research project was to develop correlations to quantify the heat transfer in the entrance region of horizontal, short circular pipes (x/D ~ 6) under uniform heat flux, for air, at Reynolds numbers ranging from 2,900 to 50,000 for combined entry. These conditions are found, for example in internal combustion engine intake runners.

Previous research in this area demonstrated that existing correlations consistently under-predict the temperatures at the intake ports. This is shown in Figure 4.19, where intake port temperature predictions from three heat transfer correlations are compared to experimental temperature data for a Diesel engine [1]. Referring to Figure 4.19, the "default" heat transfer model is Colburn's correlation, whereas the "improved" heat transfer model is Al-Arabi's correlation (both presented in Chapter 2 as part of the literature review).   That the measured temperatures are

higher than the predicted values suggest that the heat transfer from the gas in the intake runners to the cold surroundings is being over-predicted by Colburn's and Al-Arabi's correlations.
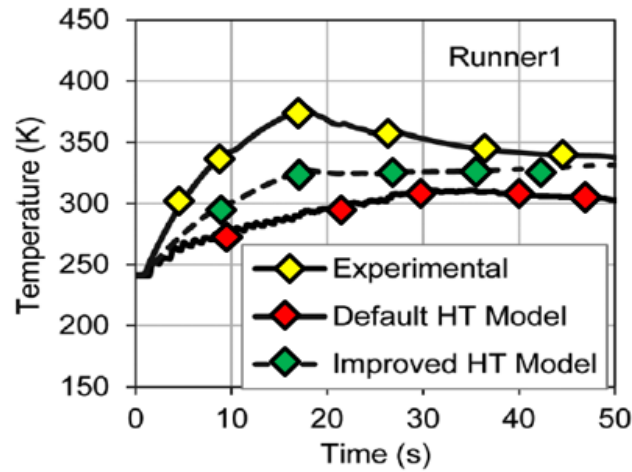
Figure 4.19: Comparison between experimentally measured and model-predicted air temperatures at the intake runners [1].

Depending on the runner, up to 25% percent discrepancy between model predictions and experimental measurements was found. The newly developed correlations, which specifically target a regime relevant to internal combustion engine intake systems, predict lower Nusselt numbers (refer to Figure 4.16) and therefore lower heat transfer coefficients. This suggests that the newly developed correlations may yield higher temperature predictions at the intake port, which is in closer alignment with the experimental results. This is yet to be validated.

4.5 Conclusions and Recommendations for Future Work

In this research, heat transfer correlations were experimentally developed for low Reynolds number lows (2,900 < Re < 50,000) in short, circular pipes (0 < x/D < 6) for air, combined entry and uniform heat flux conditions. Three entrance geometries were considered: uniform, tripped, and 90-degree entries. An energy balance was applied to quantify the average convective heat transfer, from which Nusselt numbers were calculated and correlated both with Reynolds

numbers and turbulence intensity. Axial temperature gradients were not significant due to the relatively low heat input values (see table 3.3). Prandtl number effects were, therefore, not quantified. The correlations for uniform, tripped, and 90-degree entrance, respectively, are as follows:

$$Nu = 0.099 Re^{0.582}$$

$$Nu = 0.174 Re^{0.576}$$

$$Nu = 0.0617 Re^{0.652}$$

- Overall, these correlations reveal a power-dependence of the Nusselt number on the Reynolds number, although coefficients and exponents are specific to the entrance condition.

- At a given Reynolds number, Nusselt numbers (and hence average heat transfer coefficients) is approximately 40% higher for tripped flow entry relative to uniform flow). These results may be explained by the 20% increase in turbulence intensity which, to the author's knowledge, has been directly measured and correlated to the Nusselt number for the first time.

- The empirically developed correlations were compared to existing correlations under *similar* conditions. For uniform flow entry, the developed correlations are within 27%-47% from Gnielinski's [31] and Mills' [20] over the range of Reynolds numbers investigated (i.e., 10,000<Re<50,000). Entrance conditions promoting higher turbulence (tripped flow

and 90-degree) predict Nusselt numbers in closer agreement to the aforementioned reference correlations.

Next steps will include (1) experimentally considering higher heat input values and axial temperature gradients to extend the applicability of the correlations by including Prandtl number effects, (2) conducting additional experiments focused on 2,300 < Re < 10,000 and (3) incorporating the heat transfer correlations developed into an engine intake system model and verifying their performance in terms of temperature prediction capability.

REFERENCES

[1] P. M. Kreun, C. M. Fajardo and A. Baumann, "Simulation of an Intake Manifold Preheater for Cold Engine Startup," *ASME Journal of Engineering for Gas Turbines and Power,* vol. 135, 2013.

[2] R. K. Shah and D. P. Sekulic, Fundamentals of heat exchanger design, Wiley, 2003.

[3] S. Kakaç, R. K. Shah and W. Aung, Handbook of single-phase convective heat transfer, Wiley New York et al., 1987.

[4] W. Kays, M. Crawford and B. Weigand, Convective heat transfer, McGraw-Hill, 1980.

[5] F. P. Incropera, Fundamentals of Heat and Mass Transfer, 7 ed., wiley, 2003.

[6] P. Kundu, I. Cohen, and D. Dowling, Fluid Mechanics, Elsevier Inc., 2012.

[7] F. Dittus and L. Boelter, "Heat transfer in automobile radiators of the tubular type," *International Communications in Heat and Mass Transfer,* vol. 12, no. 1, pp. 3-22, 1985.

[8] E. N. Sieder and G. E. Tate, "Heat transfer and pressure drop of liquids in tubes," *Industrial & Engineering Chemistry,* vol. 28, no. 12, pp. 1429-1435, 1936.

[9] S. W. Churchill, "Comprehensive correlating equations for heat, mass and momentum transfer in fully developed flow in smooth tubes," *Industrial & Engineering Chemistry Fundamentals,* vol. 16, no. 1, p. 109, 1977.

[10] V. Gnielinski, "New equations for heat and mass-transfer in turbulent pipe and channel flow," *International Chemical Engineering,* vol. 16, no. 2, pp. 359-368, 1976.

[11] J. E. S. a. W. M. Abraham, "Internal-Flow Nusselt Numbers for the Low-Reynolds-Number End of the Laminar-to-Turbulent Transition Regime," *International Journal of Heat and Mass Transfer,* vol. 54, no. 1, pp. 584-588, 2011.

[12] A. J. Ghajar and L.-M. Tam, "Heat transfer measurements and correlations in the transition region for a circular tube with three different inlet configurations," *Experimental Thermal and Fluid Science,* vol. 8, no. 1, pp. 79-90, 1994.

[13] A. J. Ghajar and Y. H. Zurigat, "Microcomputer-assisted heat transfer measurement/analysis in a circular tube," *Int.J.Applied Engineering Education,* vol. 7, no. 2, pp. 125-134, 1991.

[14] H. Hausen, "New equations for heat transfer in free or force flow," *Allg.Warmetchn,* vol. 9, no. 4/5, pp. 75-79, 1959.

[15] M. Al-Arabi, "Turbulent Heat Transfer in the Entrance Region of a Tube," *Heat transfer engineering,* vol. 3, no. 3, p. 76, 1982.

[16] H. D. a. K. S. Baehr, Heat and Mass Transfer, Berlin: Springer, 1998.

[17] R. G. Deissler, "Analysis of turbulent heat transfer, mass transfer, and friction in smooth tubes at high Prandtl and Schmidt numbers," 1955.

[18] M. Molki and E. Sparrow, "An Empirical Correlation for the Average Heat Transfer Coefficient in Circular Tubes," *Journal of heat transfer,* vol. 108, no. 2, p. 482, 1986.

[19] L. Boelter, G. Young, and H. Iversen, "An Investigation of Aircraft Heaters: 27-Distribution of Heat-transfer Rate in the Entrance Section of a Circular Tube," 1948.

[20] A. Mills, "Experimental investigation of turbulent heat transfer in the entrance region of a circular conduit," *Journal of Mechanical Engineering Science,* vol. 4, no. 1, pp. 63-77, 1962.

[21] M. Y, F. Kozo, T. Shinobu, and N. Masakuni, "Forced convective heat transfer in uniformly heated horizontal tubes 1st report—Experimental study on the effect of buoyancy," *International Journal of Heat and Mass Transfer,* vol. 9, no. 5, pp. 453-463, 1966.

[22] A. J. Ghajar and L.-M. Tam, "Flow regime map for a horizontal pipe with uniform wall heat flux and three inlet configurations," *Experimental Thermal and Fluid Science,* vol. 10, no. 3, pp. 287-297, 1995.

[23] S. Morcos and A. Bergles, "Experimental investigation of combined forced and free laminar convection in horizontal tubes," *Journal of Heat Transfer,* vol. 97, no. 2, pp. 212-219, 1975.

[24] T. Jackson, J. Spurlock and K. Purdy, "Combined free and forced convection in a constant temperature horizontal tube," *AIChE Journal,* vol. 7, no. 1, pp. 38-41, 1961.

[25] R. J. Goldstein, Fluid Mechanics Measurements, Taylor & Francis, 1996.

[26] F. Blair, "Hot-wire measurements of velocity and temperature fluctuations in a heated turbulent boundary layer," *Journal of Physics E: Scientific Instruments,* pp. 209-216, 1987.

[27] I. TSI, *Model 1053A Constant Temperature Anemometer Instruction Manual,* TSI Inc., 1982.

[28] S. R. Figliola and E. D. Beasley, Theory and Design for Mechanical Measurments, John Wiley & Sons, Inc., 2000.

[29] Y. Cengel, Heat Transfer a Practical Approach, McGraw-Hill, 2002.

[30] J. Q. Du, Y. Q. Zuo-Qin and D. Zhong-yuan, "Experimental Study and Numerical Simulation of Flow and Heat Transfer Performance on an Offset Plate-fin Heat Exchanger," *Heat and Mass Transfer/Waerme- Und Stoffuebertragung,* 2015.

[31] V. Gnielinski, "On heat Transfer in Tubs," *International Journal of Heat and Mass Transfer,* p. 134, 2013.

[32] C. Lomas, Fundamentals of Hot Wire Anemometry, Cambridge University Press, 1986.

[33] B. S. Pope, Turbulent Flows, Cambridge, 2008.

[34] R. R. Schmidt, "Use of Naphthalene Sublimation Technique for Obtaining Accurate Heat transfer Coefficients in Electronic Cooling Applications.," 2001. [Online]. Available: http://www.electronics-cooling.com/2001/08/use-of-naphthalene-sublimation-technique-for-obtaining-accurate-heat-transfer-coefficients-in-electronic-cooling-applications/.

[35] E. Sparrow and M. Molki, "Turbulent Heat Transfer Coefficents in an Isothermal-Walled Tube for a Built-in or Free Inlet," *International Journal of Heat and Mass Transfer,* vol. 27, no. 5, 1984.

[36] C. Bankston, "The transition from turbulent to laminar gas flow in a heated pipe," *Journal of Heat Transfer,* vol. 92, no. 4, p. 569, 1970.

[37] D. Bertsche, P. Knipper, and T. Wetzel, "Experimental investigation on heat transfer in laminar, transitional and turbulent circular pipe flow," *International Journal of Heat and Mass Transfer,* vol. 95, p. 1008, 2016.

[38] W. Grassi and D. Testi, "Heat transfer correlations for turbulent mixed convection in the entrance region of a uniformly heated horizontal tube," *Journal of heat transfer,* vol. 128, no. 10, pp. 1103-1107, 2006.

[39] S. J. Kline and F. McClintock, "Describing uncertainties in single-sample experiments," *Mechanical Engineering,* vol. 75, no. 1, pp. 3-8, 1953.

[40] H. K. Tam, L. M. Ta, and A. J. Ghajar, "Effect of inlet geometries and heating on the entrance and fully-developed friction factors in the laminar and transition regions of a horizontal tube," *Experimental Thermal and Fluid Science,* vol. 44, pp. 680-696, 2013.

[41] W. Yousef and J. Tarasuk, "Free convection effects on laminar forced convective heat transfer in a horizontal isothermal tube," *Journal of Heat Transfer,* vol. 104, no. 1, pp. 145-152, 1982.

[42] B. Zeldin and F. W. Schmidt, "Developing flow with combined forced–free convection in an isothermal vertical tube," *Journal of Heat Transfer,* vol. 94, no. 2, pp. 211-221, 1972.

[43] T. Morel, "Comprehensive design of axisymmetric wind tunnel contractions," *Journal of Fluids Engineering,* vol. 97.2, pp. 225-233, 1975.

[44] G. E. Chmielewski, "Boundary-layer considerations in the design of aerodynamic contractions.," *Journal of Aircraft,* vol. 11, no. 8 , pp. 435-438, 1974.

[45] X. e. a. Grandchamp, ""Steady laminar axisymmetrical nozzle flow at moderate Reynolds numbers: modeling and experiment."," *Journal of Fluids Engineering ,* vol. 134, no. 1, 2012.

[46] M. N. Mikhail, ""Optimum design of wind tunnel contractions."," AIAA journal , vol. 17, no. 5, pp. 471-477, 1979.

[47] TSI, "Constant Temperature Anemometer Model 1750," TSI, 2016.

Appendices

A-1: Turbulent Intensity and Velocity Profile Calculations

```
clear all

clc

close all
```

Setting the test section dimensions and probe motion step

```
pipediameter=76.2; % mm

probestep=3; % mm
```

Data Import Settings

```
%set first test number and number of tests

numTest=24;

firstTest=1;

Measurmentdirection= -1; % 1 if L-R or B-T, -1 if R-L or T-B

%Readingzero voltage

% kk=dir('C:\Users\User\OneDrive\LAB DESKTOP2\012219')

% k=0;

% s1='C:\Users\User\OneDrive\LAB DESKTOP2\020819\E';

% s2=num2str(k)

% s3='.csv';

% DataPath=strcat(s1,s2,s3)

% E0 = importdata(DataPath);

e0=0;
```

Folder root path (Ending with \)

```
filePathBase='C:\Users\User\Desktop\TestError\';
```

File name (convention: point number after name, no space)

C:\

```
fileName='RUN';

fileType='.csv';
```

Import function (for Excel sets (.xls, .csv, uses xlsread)

```
ii=ones(6,1);

for n=firstTest:1:numTest


[test(n).meanVoltage,test(n).velocity,test(n).meanvelocity,test(n).std]=Probe1(filePath
Base,fileName,n,fileType,e0);

test(n).RadialLocation=((-
Measurmentdirection*(pipediameter/2))+(Measurmentdirection*n*(probestep)))/pipediameter
;% Assumes initial position is equal to step size

end
```

Calculating the turbulence intensity

```
 for n=1:1:numTest

stdev(n)=test(n).std;

meanvelocity(n)=test(n).meanvelocity;

TurbIntensity(n)=stdev(n);

end

 int=[TurbIntensity]';

 mv=[meanvelocity]';
```

Ploting the turbulent intensity and velocity profile

Importing the probe increament

```
r = importdata('C:\Users\User\OneDrive\LAB DESKTOP2\r.xlsx');

rd=r/38.1;

 figure

subplot(2,1,1)      % add first plot in 2 x 1 grid
```

```matlab
plot(rd,TurbIntensity,'o')

grid on

 xlim([-0.5 0.5])

 ylim([0 20])

 title('Turbulent Intensity 15mm Upstream The Wind Tunnel Exit')

 xlabel('r/R')

 ylabel('Turbulent Intensity')

set(gca,'XMinorTick','on','YMinorTick','on')

 figure

 subplot(2,1,2)       % add second plot in 2 x 1 grid

plot(rd,meanvelocity,'o')       % plot using + markers

 grid on

 xlim([-0.5 0.5])

ylim([0 20])

 title('Velocity Profile 15mm Upstream The Wind Tunnel Exit')

 xlabel('r/R')

 ylabel('Mean Velocity in m/s')

 figure

 errorbar(rd,meanvelocity,stdev)

 grid on

 title('Velocity Profile 15mm Upstream The Wind Tunnel Exit')

 xlabel('r/R')

 ylabel('Mean Velocity in m/s')

 xlim([-0.5 0.5])

 ylim([0 20])
```

```matlab
%% Hot Wire Anemometry import function
function [meanVoltage,velocity,meanvelocity,stdev,numPoint] =
Probe1(filePathBase,fileName,nData,fileType,e0)
% variables for conversion assuming -ax^4+bx^3-cx^2+dx-e
a=0;
b=0;
c=6.5921;
d=-2.077;
e=0.0198;
%creation of filepath and import using xlsread (works for Excel files .csv,
%.xls, etc)
filepath=strcat(filePathBase,fileName,num2str(nData),fileType);
%keyboard
velocityVoltStruct=importdata(filepath);
% keyboard
voltage=velocityVoltStruct.data;
numPoint=size(voltage,1);
for n=1:1:numPoint
    velocityVoltDif(n)=voltage(n)-e0;

velocity(n)=((a*velocityVoltDif(n).^4)+(b*velocityVoltDif(n).^3)+(c*velocityV
oltDif(n).^2)+(d*velocityVoltDif(n))+e);
end
meanvelocity=mean(velocity);
 meanVoltage=mean(voltage);
for n=1:1:numPoint
    velocityfluct(n)=velocity(n)-meanvelocity;
end
    stdev=std(velocityfluct);
end
```

A-2 Temperature Calculations

```matlab
clear all

clc

close all
```

Input test parameters (constants)

```matlab
Lx=.5;          % length of the test section 18"

Lx2=.01

Dout=0.1099;    % out diameter of insulation

Din=0.0929;     % inner diameter of insulation

Dpout=0.0889;  % pipe out diameter

Dpin=0.0762;    % pipe in diameter

k=.03;          % air thermal conductivity
```

```matlab
    kins=.026;        % thermal conductivity of insulation

    kp=.2;            % thermal conductivity of the acrylic pipe

    emissivity=0.9; % test section surface emissivety

    segma=5.6e-8; % Stefan-Boltzmann constant
```

Test Variables

```matlab
    Voltage=16.65;% heater voltage

    Current=0.4;  % heater current

    troom=23.82;  % room air temperature

    ts=27.49;       % mean sest section surface temperature

    tm=24.84;        % mean of test section inlet and outlet temperature

    tw=23.05;       % room walls temperature

    tx2=27.36;

    ts2=33.66;    % temperature of inside surface of insulation
```

Calculating the input power

```matlab
    Qinput=Voltage*Current % input heat through the electric heater
```

Calculating conduction heat losses thrugh the insulation

```matlab
    Qlossr=(2*pi*Lx*kins*(ts-ts2))/log(Dout/Din) % heat loss through insulation in the
    radial direction

    Qlossx= (kins/Lx2)*(pi*(Dout^2-Din^2)/4)*(tx2-ts)
```

Calculating radiation heat losses

Calculating the surface area

```matlab
    Area=pi*Dout*Lx;

    Rrad=((1-emissivity)/(emissivity*Area))+(1/Area);

    Qrad=segma*((ts^4)-(tw^4))/Rrad
```

Calculating the convection heat transfer

```matlab
    Qconv=Qinput+Qlossr+Qlossx-Qrad % net heat convected by the flow
```

```
Rp=(log(Dpout/Dpin))/(2*pi*kp*Lx);

hc=1/((pi*Dpin*Lx)*(((ts2-tm)/Qconv)-Rp))

Nu=hc*Dpin/k
```

B-1: DM-65 Digital Multimeter

AC Voltage

Range (40 Hz to 400 Hz)	Accuracy
6.000 V	± (0.8% + 0.005 V)
60.00 V	± (1.2% + 0.05 V)
600.0 V	± (1.2% + 0.5 V)
1000 V*	± (1.2% + 5 V)

Input Impedance: 10 MΩ, < 100 pF

* 1000 V range is specified from 20% to 100% of range.

DC Voltage

Range	Accuracy
600.0 mV	± (0.8% + 0.5 mV)
6.000 V	± (0.8% + 0.005 V)
60.00 V	± (0.8% + 0.05 V)
600.0 V	± (0.8% + 0.5 V)
1000 V*	± (1.0% + 5 V)

Input Impedance: 10 MΩ, < 100 pF

* 1000 V range is specified from 20% to 100% of range.

B-2: Auto-Range MPJA 9903

Function	Range	Resolution	Accuracy
DC Voltage (V DC)	6V 60V 600V 1000V	1mV 10mV 100mV 1V	±(0.3% rdg + 3 dgts) ±(0.8% rdg + 3 dgts)
AC Voltage (V AC)	6V 60V 600V 750V	1mV 10mV 100mV 1V	±(1% rdg + 8 dgts)
DC Current (A DC)	600 μA 6000 μA 60mA 600mA 6A 20A	0.1 μA 1 μA 10 μA 100 μA 1mA 10mA	±(0.8% rdg + 5 dgts) ±(2% rdg +5 dgts)
AC Current (A AC)	600 μA 6000 μA 60mA 600mA 6A 20A	0.1 μA 1 μA 10 μA 100 μA 1mA 10mA	±(1.2% rdg +8dgts) ±(2% rdg + 8 dgts)
Resistance	600Ω 6kΩ 60kΩ 600kΩ 6MΩ 60MΩ	0.1Ω 1Ω 10Ω 100Ω 1kΩ 10kΩ	±(0.5% rdg +5 dgts) ±(2% rdg + 10 dgts)
Frequency (Auto Range)	11Hz to 600kHz	0.1Hz 1Hz 10Hz 100Hz 1kHz	±(0.1% rdg + 3 dgts)
Duty Cycle	0.1%~99.9%	0.1%	±(1.2% rdg + 2 dgts) pulse width: 100 μs~100ms
TEMP ℃	-20℃~300℃	1℃	±4℃
TEMP ℉	-4° F~572° F	1℉	±6° F
Capacitance (Auto Range)	60nF 600nF 6uF 60uF 100uF	0.01nF 0.1nF 1nF 10nF 100nF	±(10% rdg + 25dgts) ±(2.5% rdg + 10dgts)

Analog Output

Number of channels	2
DAC resolution	16 bits
DNL	±1 LSB
Monotonicity	16 bit guaranteed
Maximum update rate	
1 channel	250 kS/s
2 channels	250 kS/s per channel
Timing accuracy	50 ppm of sample rate
Timing resolution	50 ns
Output range	±10 V
Output coupling	DC
Output impedance	0.2 Ω
Output current drive	±2 mA
Overdrive protection	±30 V
Overdrive current	2.4 mA
Power-on state	±20 mV
Power-on glitch	±1 V for 200 ms
Output FIFO size	8,191 samples shared among channels used
Data transfers	USB Signal Stream, programmed I/O
AO waveform modes	Non-periodic waveform, periodic waveform regeneration mode from onboard FIFO, periodic waveform regeneration from host buffer including dynamic update

B-4: NI 9214 and TB-9214

Temperature Measurement Accuracy

Measurement sensitivity[5]	
High-resolution mode	
Types J, K, T, E, N	0.01 °C
Types R, S	0.03 °C
Type B	0.04 °C
High-speed mode	
Types J, K, T, E	0.10 °C
Type N	0.11 °C
Types R, S	0.36 °C
Type B	0.48 °C

B-5 Rotating Vane Anemometers Models Rva501

Velocity
Range   50 to 6,000 ft/min (0.25 to 30 m/s)
Accuracy   ±1.0% of reading ±4 ft/min (±0.02 m/s)

Area Size Input
Range
RVA501   0 to 500 ft² (0 to 46.45 m²)
RVA801   0.043 to 900 ft² (0.00399 to 90 m²)

Volumetric Flow Rate
Range   Actual range is a function of velocity and area

Temperature
Range   40 to 113°F (5 to 45°C)
Accuracy   ±2.0°F (±1.0°C)
Resolution RVA501   0.1°F (0.1°C)
Resolution RVA801   1°F (0.1°C)

Instrument Temperature Range
Operating
(Electronics)   40 to 113°F (5 to 45°C)
Storage   -4 to 140°F (-20 to 60°C)

Data Storage Capabilities (RVA501 only)
Range   12,700+ samples and 100 test IDs

Logging Interval (RVA501 only)
From 1 second to 1 hour

Time Constant (RVA501 only)
User selectable

External Meter Dimensions
RVA501   3.3 in. x 7.0 in. x 1.8 in.
               (8.4 cm x 17.8 cm x 4.4 cm)
RVA801   4.5 in. x 11 in. x 2.6 in.
               (1.2 cm x 28 cm x 6.5 cm)

Meter Weight with Batteries
RVA801   11.6 oz. (329 g)
RVA501   0.6 lbs. (0.27 kg)

Power Requirements
RVA801   9-volt battery
RVA501   Four AA-size batteries or AC adapter